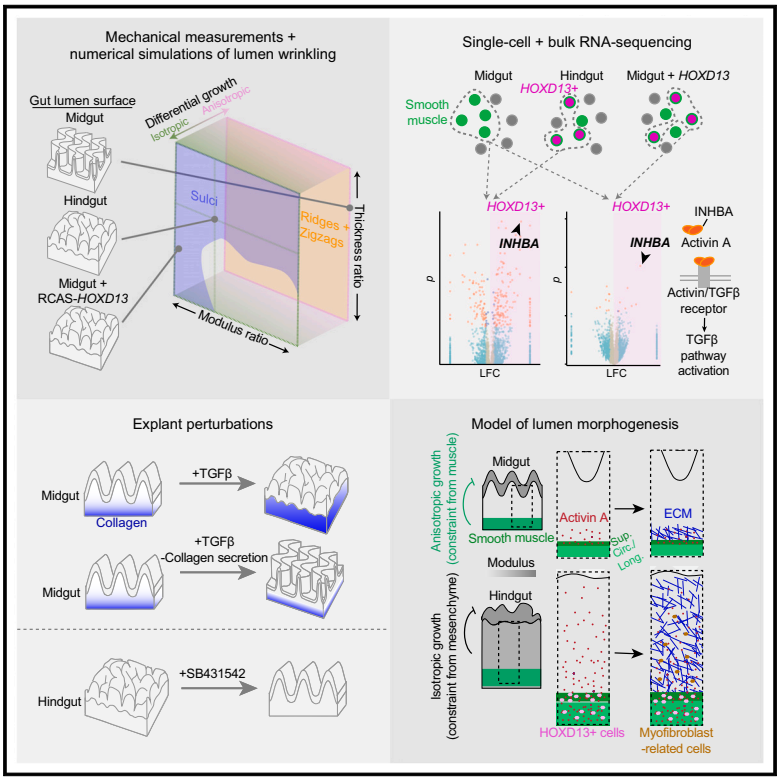
Article

Developmental Cell

Hox gene activity directs physical forces to differentially shape chick small and large intestinal epithelia

Graphical abstract



Authors

Hasreet K. Gill, Sifan Yin, Nandan L. Nerurkar, ..., Tyler R. Huycke, L. Mahadevan, Clifford J. Tabin

Correspondence

lm@seas.harvard.edu (L.M.), tabin@genetics.med.harvard.edu (C.J.T.)

In brief

Gill et al. mechanistically link *HOXD13* expression to morphogenesis of the chick hindgut epithelium. HOXD13 activity within smooth muscle induces *INHBA* expression, which causes adjacent mesenchymal cells to remodel extracellular matrix (ECM) in response to TGF-β upregulation, thus promoting the biomechanical parameters that define the hindgut morphological trajectory.

Highlights

- Mechanical properties define epithelial buckling in the developing chick intestine
- HOXD13 promotes hindgut mechanics through increased mesenchymal TGF-β signaling
- Hindgut and ectopic midgut *HOXD13*-expressing smooth muscle upregulates *INHBA*
- Mesenchymal TGF-β activation tunes mechanics via extracellular matrix remodeling

Gill et al., 2024, Developmental Cell *59*, 1–16
November 4, 2024 © 2024 Elsevier Inc. All rights reserved, including those for text and data mining, AI training, and similar technologies.
https://doi.org/10.1016/j.devcel.2024.07.012

CellPress

Please cite this article in press as: Gill et al., Hox gene activity directs physical forces to differentially shape chick small and large intestinal epithelia, Developmental Cell (2024), https://doi.org/10.1016/j.devcel.2024.07.012

Developmental Cell

CellPress

Article

Hox gene activity directs physical forces to differentially shape chick small and large intestinal epithelia

Hasreet K. Gill,[1] Sifan Yin,[2] Nandan L. Nerurkar,[3] John C. Lawlor,[1] ChangHee Lee,[1] Tyler R. Huycke,[1,4] L. Mahadevan,[2,5,*] and Clifford J. Tabin[1,6,*]

[1]Department of Genetics, Blavatnik Institute, Harvard Medical School, Boston, MA 02115, USA
[2]Harvard John A. Paulson School of Engineering and Applied Sciences, Harvard University, Cambridge, MA 02138, USA
[3]The Fu Foundation School of Engineering and Applied Science, Columbia University, New York, NY 10027, USA
[4]Department of Pharmaceutical Chemistry, University of California, San Francisco, San Francisco, CA 94158, USA
[5]Department of Physics, Department of Organismic and Evolutionary Biology, Harvard University, Cambridge, MA 02138, USA
[6]Lead contact
*Correspondence: lm@seas.harvard.edu (L.M.), tabin@genetics.med.harvard.edu (C.J.T.)
https://doi.org/10.1016/j.devcel.2024.07.012

SUMMARY

Hox transcription factors play crucial roles in organizing developmental patterning across metazoa, but how these factors trigger regional morphogenesis has largely remained a mystery. In the developing gut, Hox genes help demarcate identities of intestinal subregions early in embryogenesis, which ultimately leads to their specialization in both form and function. Although the midgut forms villi, the hindgut develops sulci that resolve into heterogeneous outgrowths. Combining mechanical measurements of the embryonic chick intestine and mathematical modeling, we demonstrate that the posterior Hox gene *HOXD13* regulates biophysical phenomena that shape the hindgut lumen. We further show that HOXD13 acts through the transforming growth factor β (TGF-β) pathway to thicken, stiffen, and promote isotropic growth of the subepithelial mesenchyme—together, these features lead to hindgut-specific surface buckling. TGF-β, in turn, promotes collagen deposition to affect mesenchymal geometry and growth. We thus identify a cascade of events downstream of positional identity that direct posterior intestinal morphogenesis.

INTRODUCTION

Hox genes were first identified in *Drosophila*, where they were shown to form a combinatorial code that specifies the identity and morphogenesis of the arthropod segments.[1,2] With the discovery of the conserved homeobox domain[3,4] and highly related genes in vertebrates,[5,6] it was soon after proposed that an overlapping pattern of Hox gene activity may serve as a code for establishing differential vertebral morphologies[7]: a model that has since been shown to be essentially correct.[8] Indeed, we now know that Hox genes play crucial roles in the differential anterior-posterior patterning of a variety of vertebrate embryonic tissues, including the developing gastrointestinal (GI) tract. It is striking, however, that more than 30 years later, the downstream interplay of genetic, cellular, and mechanical processes that Hox genes act through to direct regional differences in morphology remains a black box. In fact, though studies in *Drosophila* have uncovered Hox-regulated cellular and mechanical phenomena that drive organogenesis, such mechanistic knowledge is virtually nonexistent for vertebrate organ systems.[9,10]

Regionalized Hox gene expression in the GI tract—which forms as a uniform tube and differentiates into morphologically distinct organ structures required for digestion—is a broadly conserved feature across taxa.[11] In vertebrates, Hox paralog groups 9–13 are expressed in a nested set of overlapping domains with distinct regional boundaries demarcating domains of the hindgut and midgut.[12–14] *Hoxd13* loss of function destroys the muscular apparatus of the anal sphincter in the mouse, and suppression of HOXA13 in the chick causes hindgut and cloacal atresia.[15–18] Most striking, however, is the finding that *HOXD13* overexpression in the chick midgut is sufficient to replace the epithelial lining with one resembling that of the hindgut and produce the acid mucin-secreting cells typical of the large intestine.[19] *HOXD13* is, thus, critically involved in multiple aspects of hindgut development—but how it affects tissue properties to influence morphogenesis has, once again, remained a black box.

The mechanisms underlying differences in morphogenesis of the distinct functional domains of the gut have remained unresolved, though progress has been made in understanding the morphogenesis of midgut epithelium. In mice, humans, and chickens, the lumen of the mature midgut-derived small intestine contains long finger-like epithelial projections called villi, while the lining of the hindgut-derived large intestine forms superficial epithelial folds that have been referred to as "villus-like

All rights are reserved, including those for text and data mining, AI training, and similar technologies.

Please cite this article in press as: Gill et al., Hox gene activity directs physical forces to differentially shape chick small and large intestinal epithelia, Developmental Cell (2024), https://doi.org/10.1016/j.devcel.2024.07.012

structures," "colonic villi," or "epithelial cuffs."[20–24] The villi of the chick small intestine form through a stepwise process in which the gut endoderm and subjacent mesenchyme first fold into longitudinal ridges, followed by zigzags and, finally, ordered arrays of villi that emerge via localized proliferation.[25] The majority of this process is orchestrated by the sequential differentiation of distinct smooth muscle layers, the first oriented circumferentially and the latter two oriented longitudinally. These act to restrict the expansion of the growing epithelium and mesenchyme, creating the compressive stresses that lead to their buckling.

This model raises a conundrum, however, as the same three smooth muscle layers arise in the same sequence in the hindgut, yet it achieves a very different epithelial morphology.[26] One possible answer would lie in different mechanical properties and differential growth-induced strains in the two developing gut segments, as these parameters determine the way a tissue deforms when constrained. This begs the question of how the properties of the developing midgut and hindgut differ physically, whether such differences can explain differential epithelial morphogenesis, and, if so, how the hindgut achieves unique physical properties in the first place. Here, we identify how mechanical and growth parameters in the embryonic chick midgut and hindgut give rise to their unique morphologies. We further uncover that these regional tissue mechanics are specified by upstream *HOXD13* expression, which patterns the tissue through transforming growth factor β (TGF-β) signaling.

RESULTS

Distinct stepwise morphogenesis of the epithelia in the midgut and hindgut

In the midgut, the smooth endodermal lining at embryonic day (E) 8 transforms into a series of ridges at E12, zigzags at E14, and protovilli—bulges that prefigure final villi locations—by E18[25] (Figures 1A and 1B). By contrast, the first observable deformation of the luminal surface of the hindgut occurs at E12 when it forms a superficial wrinkling pattern that becomes extensively branched by E14 and evolves into cuffs by E16 (Figure 1A). While long, thin villi display crystalline regularity in their shapes and arrangement,[27] cuffs are shorter, wider, heterogeneous in size, and appear spatially disordered (Figures 1A and 1E).

Simultaneously, in the E14 hindgut lumen, a secondary buckling pattern that includes both the inner epithelial endoderm (hereafter simply referred to as "endoderm") and the subepithelial layer of mesenchyme (hereafter, "mesenchyme") appears[26] (Figure 1D). This is also the time when the inner longitudinal layer of smooth muscle differentiates (Figures 1B and 1D), which forms in a pattern of periodic deformations distanced from the subjacent circumferential layer—a configuration maintained as the lumen surface develops cuffs (Figure 1E). By comparison, there is no such second-order folding in the midgut, and the inner longitudinal layer of smooth muscle forms a flat band beneath the epithelial folds.

The fact that muscles are thicker in the hindgut and that each differentiates 1–2 days earlier should only make them more effective in driving the morphological transformations observed in the midgut (Figures 1B and 1D). We therefore hypothesized that geometric and mechanical properties of the inner layers themselves differ between the midgut and hindgut, thus affecting how they deform in response to physical constraints from muscle.

The developing hindgut and midgut have distinct physical properties

The reticulated grooves that first appear on the luminal surface of the hindgut resemble sulci, which are unique, nonlinear surface instabilities that have recently been studied in the context of the brain, though they appear widely in nature.[28–30] Extensive theoretical analyses would suggest that sulci in the gut may emerge when the endoderm-mesenchyme composite is compressed equibiaxially (through transversely isotropic expansion), where the modulus ratio of the two layers is low (i.e., they are equally stiff, or the endoderm is softer).[31–35] To test this possibility, we measured physical parameters predicted to collectively determine how the midgut and hindgut lumen surfaces will deform: differential growth, geometric features, and stiffnesses of inner endoderm and mesenchyme layers.

We first measured strain in these layers resulting from differential growth in each axis relative to muscle (Figures 2A and S1A) (STAR Methods). As expected, the midgut initially develops strain only circumferentially (negative values in Figure 2B, left), reflecting the circumferential compression that forces formation of longitudinal ridges. Subsequently, between E12 and E14, longitudinal compression appears, concomitant with differentiation of the outer longitudinal layer of smooth muscle and formation of zigzags (Figure 2B, right), while at this stage the rate of circumferential strain acquisition does not increase (i.e., the slope remains the same). Therefore, within each growth period (E8–E12, E12–E14, E14–E18), midgut growth is anisotropic, as previously reported.[25,36] Consistent with the theoretical analyses of sulci formation, the hindgut instead gradually develops compression on both axes nearly simultaneously, resulting in equibiaxial growth during most of lumen morphogenesis (Figure 2B).

Along with stiffness (modulus) ratio, the ratio of endoderm to mesenchyme thickness influences the distribution of stress within the endoderm-mesenchyme composite as it grows and is constrained by muscle. For example, a very thin and relatively stiff endoderm layer will buckle differently from a thick and soft layer even if growing at the same rate, with identical constraints. Tissue thickness measurements (Figures 2A and S1A) revealed that both the endoderm and mesenchyme layers are ultimately thicker in the hindgut than in the midgut (Figures S1B and S1C). Notably, during the appearance of sulci from E12 to E14, the hindgut thickness ratio drops significantly as the mesenchyme drastically thickens, which does not occur in the midgut (Figure 2C).

Given that E12–E14 is the key time frame when the midgut and hindgut develop distinct biaxial morphologies (dark gray in Figure 2B), we next measured Young's moduli of the endoderm and mesenchyme layers at E14 (Figure S1A) (STAR Methods). We first observed that the endoderm is softer in the hindgut at E14 (Figure S1B), while mesenchyme modulus is higher in the hindgut during the time frame when sulci develop (Figure S1C). Thus, at the critical time when the midgut forms zigzags, but the hindgut forms sulci, the modulus ratio between the endoderm and mesenchyme is high in the midgut and low in the hindgut

Please cite this article in press as: Gill et al., Hox gene activity directs physical forces to differentially shape chick small and large intestinal epithelia, Developmental Cell (2024), https://doi.org/10.1016/j.devcel.2024.07.012

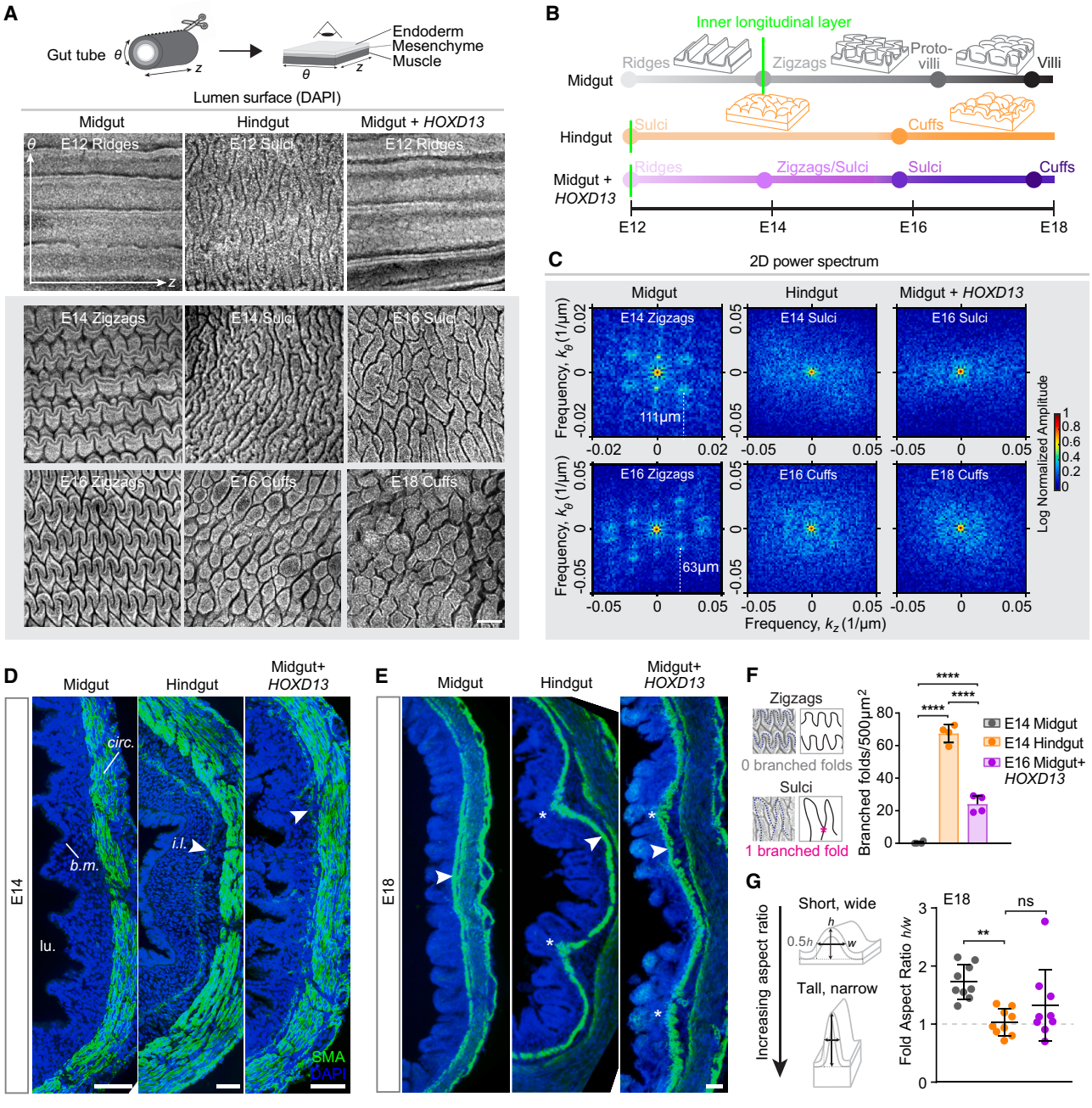


Figure 1. The chick hindgut adopts distinct lumen wrinkling patterns from the midgut, which are recapitulated with *HOXD13* misexpression

(A) Lumen surface imaging method and images of the midgut, hindgut, and RCAS-*HOXD13* midgut ("Midgut + *HOXD13*") at the indicated time points. Scale bars, 100 μm.

(B) Timeline of lumen morphogenesis for each condition. Color gradient shapes indicate timescales of transitions (steep, abrupt; shallow, prolonged).

(C) Power spectral densities for images within the gray filled box in (A). Dashed lines, characteristic wavelength values on the longitudinal axis (z).

(D and E) Gut transverse sections at E14 (D) and E18 (E). SMA, alpha smooth muscle actin; b.m. and line, basement membrane; lu., lumen; circ., circumferential muscle layer; i.l. and arrowhead, inner longitudinal muscle layer; asterisk, secondary large-scale fold. Scale bars, 50 μm.

(F and G) (F) Branched folds per 500 μm^2 (n = 4 images, 2 embryos/condition) and (G) fold aspect ratios at E18 only (n = 9 folds, 1 embryo/condition).

(F) and (G) One-way ANOVA, Tukey's MCT. Error bars, SEM. **$p < 0.01$; ****$p < 0.0001$.

See also Figure S3.

Please cite this article in press as: Gill et al., Hox gene activity directs physical forces to differentially shape chick small and large intestinal epithelia, Developmental Cell (2024), https://doi.org/10.1016/j.devcel.2024.07.012

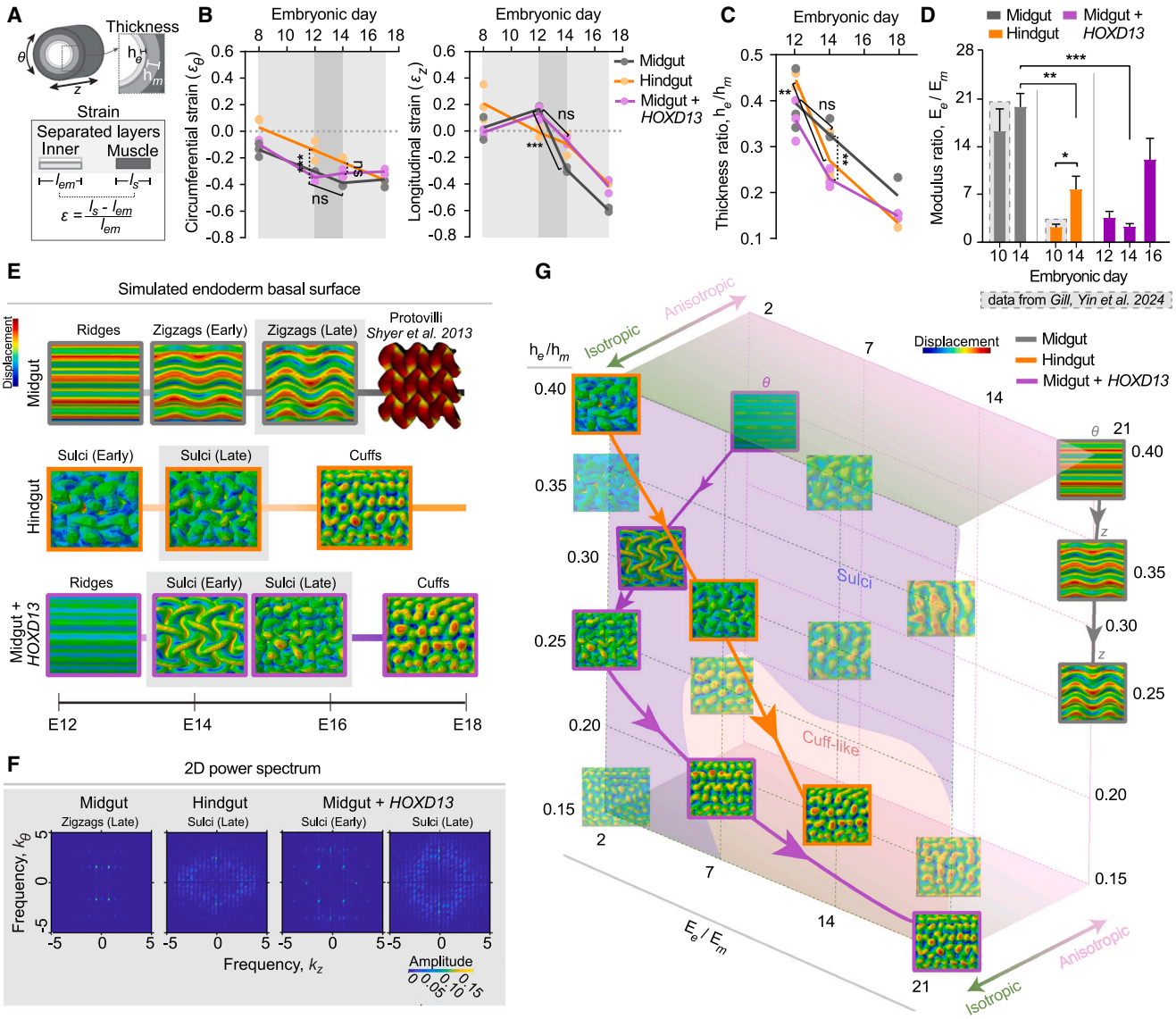


Figure 2. Hindgut mechanical properties diverge from those of the midgut and are promoted by *HOXD13* activity

(A) Measurement of tissue thicknesses, h, and strains, ε.

(B) Differential growth on each axis with relevant time frames in gray. Dark gray, biaxial buckling transition (n = 3 gut segments, 2 embryos/condition, for each time point).

(C and D) (C) Thickness ratios (n = 2–3 sections, 2 embryos/condition) and (D) Young's modulus values (each stage: n = 4–6 gut segments, 4 embryos/condition; see Figure S1). E10 data from Gill et al.[26] are reprinted for comparison to the E12 RCAS-*HOXD13* midgut.

(E) Numerical simulation results at successive stages of lumen morphogenesis (Figure 1B; Table S1).

(F) Power spectra corresponding to gray filled boxes in (E).

(G) Three-dimensional parameter space for lumen morphogenesis empirically determined from 27 numerical simulations. Lines, experimental trajectories; boxes, simulation results (STAR Methods). (B) and (C) Two-way ANOVA, Tukey's MCT. Dotted brackets, comparisons between conditions; solid brackets, comparisons between stages. ***$p < 0.001$. (D) E14: one-way ANOVA, Tukey's MCT. **$p < 0.01$; ***$p < 0.001$. (D) Hindgut: unpaired, two-tailed t test. Error bars, propagated SEM (STAR Methods). **$p < 0.01$.

See also Figure S1 and Table S1.

(Figure 2D). We also noted that the modulus ratio in the hindgut increases over time from E8 onward (Figures 2D and S1D).

Taken together, the elastic, geometric, and growth properties of the hindgut are both distinct from those of the midgut and qualitatively consistent with theoretical work on the emergence of creased sulci patterns.

A mathematical model incorporating measured physical parameters recapitulates midgut and hindgut morphogenesis

Despite similarities between our observations and theoretical expectations, determining whether measured values explain different lumen patterns required turning to computational

Please cite this article in press as: Gill et al., Hox gene activity directs physical forces to differentially shape chick small and large intestinal epithelia, Developmental Cell (2024), https://doi.org/10.1016/j.devcel.2024.07.012

modeling. We therefore constructed a mathematical model based on a widely used differential growth framework,[25,31,35] but now combined with experimentally measured physical parameters over time (STAR Methods).

The deformation gradient that defines shape change in morphoelasticity theory is decomposed into spatiotemporal growth and elastic tensors, where the growth tensor was fitted to differential growth behaviors of the midgut and hindgut. We assigned stepwise anisotropic growth to the midgut and transversely isotropic growth, or equibiaxial growth along the circumferential and axial directions, to the hindgut (Table S1). Combined with measured thickness and modulus ratios at each stage of lumen wrinkling, our model predicted the distinct morphological trajectories of the midgut and hindgut. As expected, stepwise anisotropic growth in the context of a relatively high modulus ratio and moderately decreasing thickness ratio yields ridges followed by zigzags (Figure 2E). By contrast, a low modulus ratio with simultaneously increasing longitudinal and circumferential growth results in sulci at both high and low thickness ratios (Figures 2E and 2G). Further exploration of the parameter space defined by these three characteristics (Figure 2G) revealed that, indeed, sulci appearance is driven by transversely isotropic growth.

Most striking from our simulations, however, was the observation that in the high modulus ratio and low thickness ratio regime, the surface pattern becomes limited to spatially segmented outgrowths resembling cuffs instead of labyrinthine sulci (Figure 2G). Given the trend of increasing modulus ratio and drastically decreasing thickness ratio in the hindgut, its endogenous morphological trajectory ultimately lands in this predicted "cuff-like" state (Figures 2C–2E, 2G, and S1D). Thus, unlike in the midgut, where the final stages of villus outgrowth cannot be explained by a continuum-level mechanical model of lumen wrinkling,[25] our model captures all major steps of hindgut morphogenesis from bulk biophysical parameters alone and further indicates that these properties are sufficient to drive lumen morphogenesis.

HOXD13 misexpression in the midgut transforms luminal folding to a hindgut-like pattern

With a biomechanical understanding of chick intestinal lumen wrinkling in hand, we next turned our focus to the genetic regulation of these patterns. Prior to and at the time of hindgut morphogenesis, *HOXD13* is expressed throughout the developing hindgut mesoderm and endoderm (Figures S2A and S2B). Previous work showed that when misexpressed in the developing midgut, *HOXD13* transforms the luminal folding pattern into a phenocopy of the wild-type hindgut.[19] To assess this phenotype in more detail, a replication competent retroviral vector transducing *HOXD13* (RCAS-*HOXD13*) was electroporated into the midgut lateral plate mesoderm[37] (STAR Methods). At early stages of gut morphogenesis, the infected midguts look indistinguishable from controls (Figure 1A). However, when the hindgut forms sulci and the midgut adopts a zigzag configuration at E14, the *HOXD13*-expressing midgut (Figure S2C) displays an intermediate phenotype between the two (Figures 1A and S3A). By day 16, the *HOXD13*-expressing midgut ridges have transformed to a sulci pattern like that of the day 14 hindgut, albeit with a 2-day delay (Figures 1A and 1B), and by day 18, the *HOXD13*-expressing midguts have formed short and wide cuffs like those of the day 16 or 18 hindgut (Figures 1A, 1E, and 1G).

Moreover, the E18 *HOXD13*-expressing midguts display the secondary buckling characteristic of the hindgut at this stage, wherein the inner longitudinal layer of smooth muscle shifts away from the circumferential muscle boundary (Figure S3D) and forms periodic folds along with the adjacent mesenchyme, as in the hindgut (Figure 1E). Finally, in the *HOXD13*-expressing midgut, the inner longitudinal layer has already formed at E14, recapitulating earlier muscle differentiation of the hindgut (Figures 1B and 1D).

To quantitatively determine if HOXD13 activity is sufficient to posteriorize midgut folding and smooth muscle differentiation, we applied methods of assessing properties of wrinkling patterns in the midgut, hindgut, and *HOXD13*-expressing midgut (STAR Methods), comparing the E16 RCAS-*HOXD13* midgut (sulci) to E14 midgut (zigzags) and hindgut (sulci) and the E18 RCAS-*HOXD13* midgut (cuffs) to the E16 midgut (late zigzags) and hindgut (cuffs) (Figures 1A and 1B). First, while zigzag folds in the E14 midgut are essentially unbranched, we observe significant branching in both the E14 hindgut and E16 *HOXD13*-expressing midgut (Figure 1F). Furthermore, both hindgut cuffs and *HOXD13*-expressing midgut cuffs show relatively higher spatial disorder in the surface arrangements of outgrowths (Figure S3C) and lower aspect ratios than villi (Figure 1G). Finally, while Fast Fourier Transform (FFT) and autocorrelation plots reflect the periodic patterns present in midgut patterns across time points, the hindgut has a diffuse spectral density profile at all stages, and autocorrelation amplitudes present only mild evidence of longitudinal periodic wrinkling (Figures 1C and S3B). The E16 and E18 *HOXD13*-expressing midguts, strikingly, display 2D power spectra and autocorrelation profiles like those of the hindgut 2 days earlier in each case (Figures 1C and S3B). Thus, ectopic expression of *HOXD13* drives the midgut toward a hindgut-like morphology—namely, branched wrinkling, spatially disordered and squatter final outgrowths, and diminished pattern periodicity.

HOXD13 modulates mechanical properties of the developing gut tube

To test whether HOXD13 alters lumen morphogenesis by modulating the physical parameters that distinguish the midgut from the hindgut, we again measured differential growth, stiffness, and geometric features of inner endoderm and mesenchyme layers, but now in *HOXD13*-expressing midguts. Consistent with it initially forming midgut-like ridges, circumferential differential growth of the *HOXD13*-expressing midgut is indistinguishable from that of the wild-type midgut until E12 (Figure 2B, left). However, the dramatic increase in longitudinal compression that normally forces buckling into zigzags between E12 and E14 in the midgut is dampened with *HOXD13* misexpression, making differential growth less anisotropic during this period (Figure 2B, right). Subsequent midgut + *HOXD13* differential growth trajectories are closer to or overlap with those of the hindgut, suggesting, once again, that the biaxial buckling transition is the key time point when the wild-type and transformed midgut patterns diverge and that this deviation in the *HOXD13*-expressing midgut pattern evolution is marked by loss of anisotropic growth.

Like the hindgut, the *HOXD13*-expressing midgut mesenchyme becomes notably thicker as the lumen develops sulci and cuffs, which lowers the thickness ratio relative to the

Please cite this article in press as: Gill et al., Hox gene activity directs physical forces to differentially shape chick small and large intestinal epithelia, Developmental Cell (2024), https://doi.org/10.1016/j.devcel.2024.07.012

wild-type midgut (Figures 2C and S1C). Higher mesenchyme modulus also leads to a lower endoderm-to-mesenchyme modulus ratio compared with the wild-type midgut—in fact, the ratio at E14 is nearly identical to the hindgut modulus ratio just a few days prior at E10[26] (Figures 2D and S1C). Therefore, we conclude that both thickening and stiffening of the mesenchyme, without changes to endoderm properties, are sufficient to imbue the RCAS-*HOXD13* midgut with hindgut-like physical and geometric characteristics.

To verify that the physical parameters altered by *HOXD13* misexpression can explain the hindgut-like phenotype we observed, we examined the pattern trajectory predicted by our computational model. We first observed that a transition to isotropic growth with a low modulus ratio, analogous to the transitional E14 morphology in Figure S3A, generated an ordered periodic pattern of sulci instead of zigzags from subtle initial ridges (Figures 2E–2G). Subsequent models generated sulci like those of hindgut simulations, with diffuse and circular power spectra (Figures 2E and 2F). As in the hindgut, the *HOXD13*-expressing modulus ratio trends upward afterward, which, in conjunction with a lower thickness ratio at E18, leads to segmentation of sulci into cuffs (Figures 2D, 2G, and S1D).

We conclude, therefore, that the breakdown of epithelial ridges into sulci by HOXD13 is largely achieved through thickening and stiffening of the developing gut mesenchyme—rendering lower modulus and thickness ratios between the endoderm and mesenchyme—and a shift to isotropic growth; cuffs then resolve through a subsequent increase in modulus ratio and decrease in thickness ratio (Figure 2G). However, though this finding advanced our understanding of the role of HOXD13 in the hindgut, the mechanism by which this Hox transcription factor alters tissue material and geometric properties remained unclear.

TGF-β signaling is upregulated in hindgut and *HOXD13*-expressing midgut subepithelial mesenchymal cells

To investigate pathways potentially regulated by HOXD13 to establish gut morphology, we performed bulk-RNA sequencing (RNA-seq) to identify genes commonly differentially expressed in the mesodermal layers of sulci/cuff-forming lumens of both the developing hindgut and *HOXD13*-expressing midgut at E12 and E14 (STAR Methods).

Filtering for genes differentially expressed in both the hindgut and *HOXD13*-expressing midgut relative to the wild type at both time points yielded a list of 62 genes (Figure S4A), of which 25% (16/62) were found to be involved at various levels in the TGF-β superfamily[38–42] (Figures 3A–3C, S4B, and S4C). Focusing on three of the most relevant and significantly upregulated genes, *INHBA*, *THBS2*, and *CFC1*, we performed hybridization chain reaction fluorescence *in situ* hybridization (HCR-*FISH*) and found that all three genes show increased expression in the mesenchyme and/or muscle (Figures 3D, 3E, and S4D). Accordingly, at both E12 and E14, we observed higher proportions of pSMAD2-positive nuclei (a readout of TGF-β pathway activation[38,41,42]) in mesenchymal cells of the hindgut and *HOXD13*-expressing midgut (Figures 3F and 3G). The staining patterns in these conditions revealed that TGF-β activity also decreases to a lesser extent from the inner edge of the circumferential muscle layer to the basement membrane (Figure S4E). Together, these results suggest that *HOXD13* expression in the gut is sufficient to instigate TGF-β pathway activation in the subepithelial mesenchyme, where hindgut and *HOXD13*-expressing midgut physical properties differ from the wild-type midgut.

HOXD13 expression in smooth muscle cells leads to tissue-autonomous upregulation of *INHBA*

To delineate the location within the gut mesoderm where HOXD13 promotes TGF-β pathway activation and to determine whether it does so cell autonomously, we next performed single-cell RNA-seq (scRNA-seq) of the hindgut at E15, when it is mechanically, morphologically, and transcriptionally distinct from the midgut. Three smooth muscle clusters showed the highest expression of *HOXD13* in the mesoderm (Figure 4A): circumferential and longitudinal layers that express markers of mature, contractile smooth muscle ("circ./long."), a transcriptionally distinct population of cells on the inner, "superficial" ("sup.") edge of the circumferential layer,[43] and a cycling subset ("G2/M") that we excluded from further analysis (Figure 4B). These results are consistent with the sites of *HOXD13* endogenous expression in the hindgut (Figure S2B), making the smooth muscle a reasonable candidate for the site of TGF-β gene regulation.

Widespread and sustained RCAS-*HOXD13* overexpression in the midgut led to drastic changes to the organization and development of tissues, obscuring the direct consequences of *HOXD13* transcriptional activity in mesodermal cells. To discern how *HOXD13* independently changes the transcriptional profiles of smooth muscle cells that are otherwise similar to corresponding control cells, we ectopically expressed it over a shorter time frame and in a sparse, inducible manner (Figure S5A) (STAR Methods). We then asked which genes are commonly differentially expressed in *HOXD13*+ midgut and hindgut cells relative to midgut control cells of the same type.

Pseudobulk RNA-seq comparing smooth muscle cells between conditions revealed that in circumferential/longitudinal smooth muscle, the Activin A ligand subunit *INHBA* (which was also a top hit in our bulk analysis) is highly differentially expressed in hindgut *HOXD13*-expressing cells compared with midgut control cells (Figures 4C and 4D). *INHBA* also had the lowest *p* value and highest log fold change in midgut circ./long. smooth muscle cells with ectopic *HOXD13* expression vs. midgut empty vector control cells (Figures 4C, 4D, and S5B). Importantly, analysis of *ACTG2* expression showed that midgut *HOXD13*+ cells retain expression of the appropriate cluster markers and thus did not change their cell type identities (Figure 4E). Other sites of *HOXD13* endogenous and ectopic expression did not show the same degree of concordance between midgut vs. *HOX*+ hindgut and midgut vs. *HOX*+ midgut differentially expressed genes (Figures S5C–S5E). These results suggest that *HOXD13* expression in hindgut smooth muscle induces expression of *INHBA* (which is also recapitulated in the RCAS-*HOXD13* midgut: Figure 3E, arrowheads). Extracellular Activin A assembled from INHBA subunits then presumably signals in a paracrine manner to the adjacent mesenchyme to stimulate the TGF-β pathway.

Modulating TGF-β pathway levels toggles lumen patterns between midgut and hindgut morphologies

Our data strongly support a role for HOXD13 in stimulating spatially patterned mesenchymal TGF-β pathway activity via

Please cite this article in press as: Gill et al., Hox gene activity directs physical forces to differentially shape chick small and large intestinal epithelia, Developmental Cell (2024), https://doi.org/10.1016/j.devcel.2024.07.012

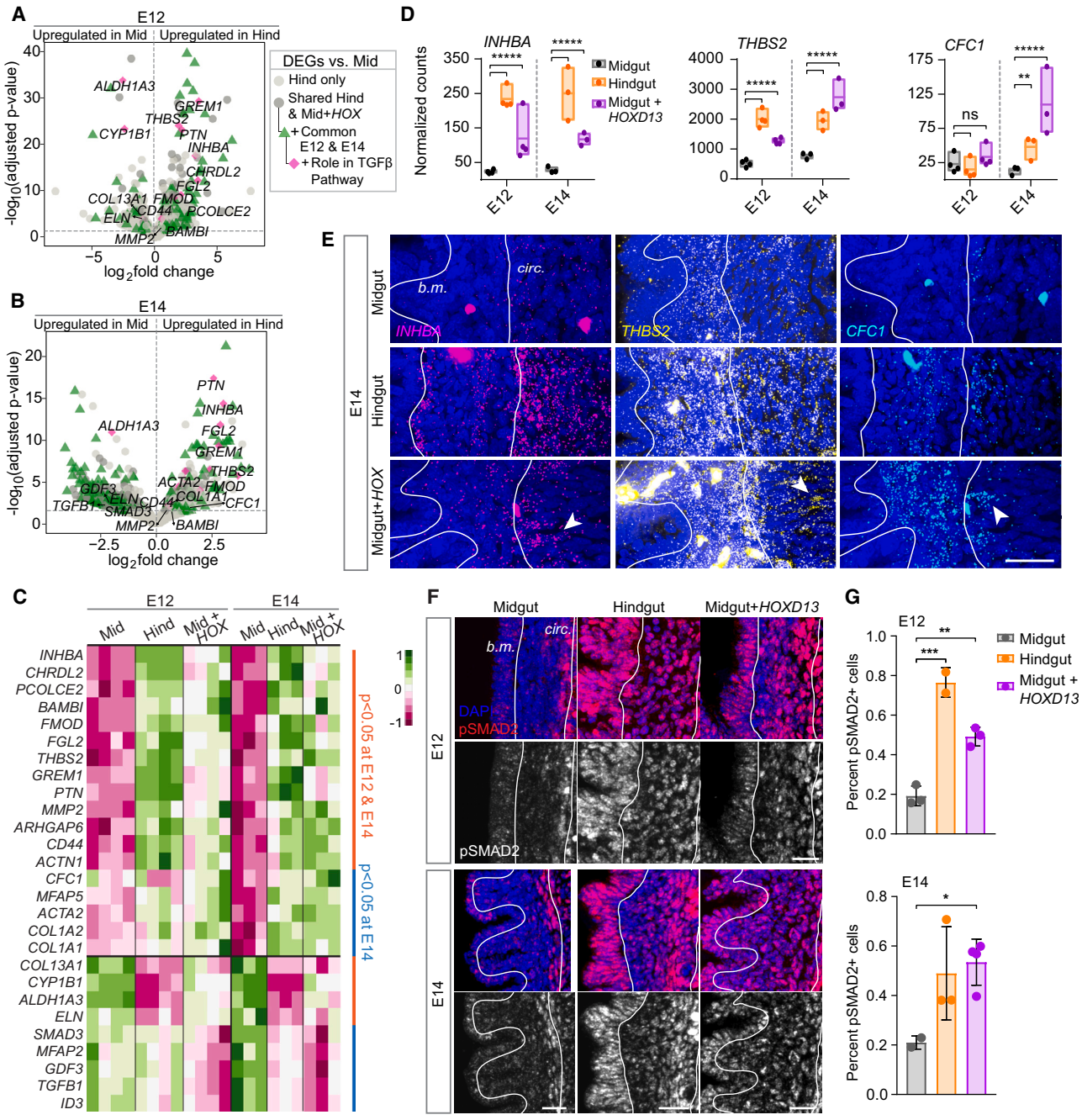


Figure 3. TGF-β signaling is upregulated in the hindgut and RCAS-*HOXD13* subepithelial mesenchyme

(A and B) Differentially expressed genes ("DEGs") between hindgut and midgut mesodermal layers at (A) E12 and (B) E14. Dot shapes/colors indicate successive subsets of DEGs (STAR Methods).

(C) Heatmap of final subset of TGF-β pathway genes corresponding to pink diamonds in (A) and (B), with orange and blue bars indicating in which stages genes were differentially expressed.

(D) Normalized counts for three TGF-β genes of interest ($n = 4$ and 3 embryos/condition at E12 and E14, respectively; DESeq2 Wald test with Benjamini-Hochberg [BH] p adjustment). $^{**}p < 0.01$; $^{*****}p < 0.00001$; ns, not significant.

(E) HCR-*FISH* at E14. Area between white lines, subepithelial mesenchyme; arrowheads, smooth muscle cells; b.m., basement membrane; circ., circumferential muscle layer; scale bars, 50 μm.

(F and G) (F) pSMAD2 immunostains, scale bars, 20 μm, and (G) proportion of pSMAD2-positive cells in the subepithelial mesenchyme (n = 3–4 sections, 2 embryos/time point). One-way ANOVA, Tukey's MCT. Error bars, SEM. $^{*}p < 0.05$; $^{**}p < 0.01$; $^{***}p < 0.001$.

See also Figure S4.

Please cite this article in press as: Gill et al., Hox gene activity directs physical forces to differentially shape chick small and large intestinal epithelia, Developmental Cell (2024), https://doi.org/10.1016/j.devcel.2024.07.012

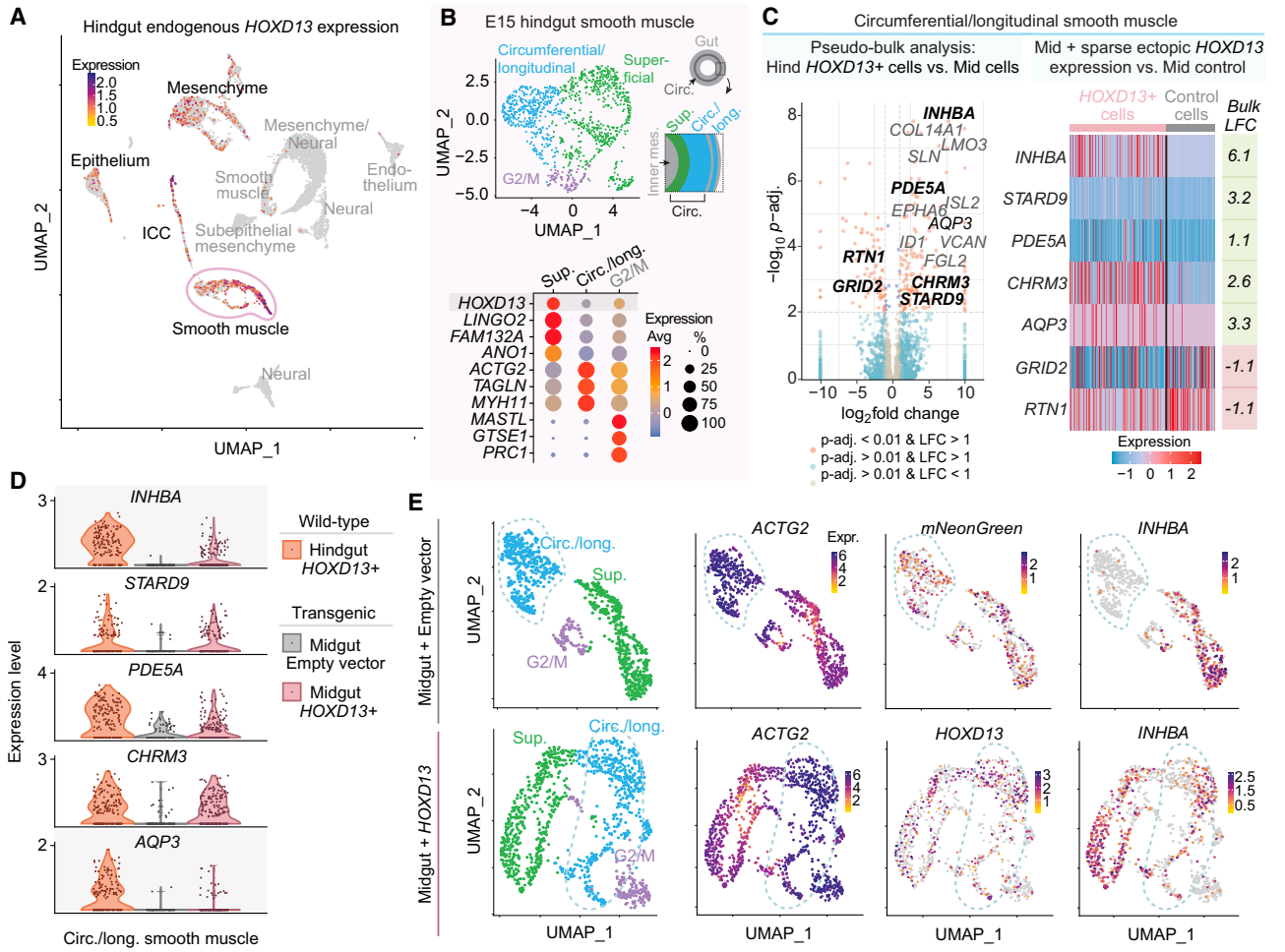


Figure 4. *HOXD13* expression in smooth muscle leads to tissue-autonomous upregulation of INHBA

(A) *HOXD13* expression at E15 (n = 9,022 cells, 2 embryos, 19 clusters). Pink outline, clusters where *HOXD13* is differentially expressed. ICC, interstitial cells of Cajal. Wilcoxon rank-sum test with Bonferroni p adjustment, p adj < 0.00001.

(B) Re-clustered smooth muscle cell populations from (A) (n = 1,093 cells) and expression of *HOXD13* alongside the top 3 markers per cluster.

(C) Differential gene expression analysis (quasi-likelihood ratio test [LRT], Gamma-Poisson fit, BH p adjustment) for circ./long. cells of the control midgut (n = 83 cells) and hindgut (n = 142 cells). Heatmap containing transgenic (*mNeonGreen*+) midgut control cells (n = 83, 2 embryos) and transgenic midgut *HOXD13*+ cells (n = 159, 2 embryos) from their respective circ./long. smooth muscle clusters. Genes and log fold change (LFC) values come from pseudobulk differential gene expression analysis in Figure S5B.

(D) Expression levels of the top 5 shared DEGs in circ./long. muscle cells for each condition. Gray boxes, genes also discovered via bulk-RNA sequencing (Figure 3C).

(E) Smooth muscle subclusters and feature plots for the midgut control (n = 919 cells, 2 embryos) and midgut + *HOXD13* (n = 1,188 cells, 3 embryos).

See also Figure S5.

regulation of ligand expression in the adjacent smooth muscle. We therefore next modulated TGF-β signaling in *ex vivo* culture to ask if this pathway is relevant to specifying lumen morphology. When cultured in the presence of recombinant mouse TGF-β1 or recombinant Activin A, the midgut developed a labyrinthine surface folding pattern more like the sulci and cuffs of the hindgut than ridges or zigzags of the midgut (Figures 5A and S6H), which we verified quantitatively (Figures 5C, 5E, S6A, and S6B).

To then determine whether TGF-β signaling is necessary in the hindgut to promote sulci and cuff morphogenesis, we cultured hindgut explants with SB431542, a TGF-β receptor inhibitor. Remarkably, sharp and smooth ridges with circumferential periodicity—a morphology never seen in the hindgut development trajectory—formed instead of branched sulci, consistent with a role for TGF-β in lumen shaping (Figures 5B, 5C, 5E, S6A, and S6B). SB431542 treatment also produced sharp ridges instead of sulci in the RCAS-*HOXD13* midgut (Figure S6K). TGF-β signaling downstream of HOXD13 thus appears to guide the morphological trajectory of the large intestine toward sulci and cuffs.

TGF-β activation is necessary and sufficient to promote hindgut mechanical properties and equibiaxial differential growth

To ask whether TGF-β regulates the same tissue properties as HOXD13 to influence lumen shaping, we again measured

Please cite this article in press as: Gill et al., Hox gene activity directs physical forces to differentially shape chick small and large intestinal epithelia, Developmental Cell (2024), https://doi.org/10.1016/j.devcel.2024.07.012

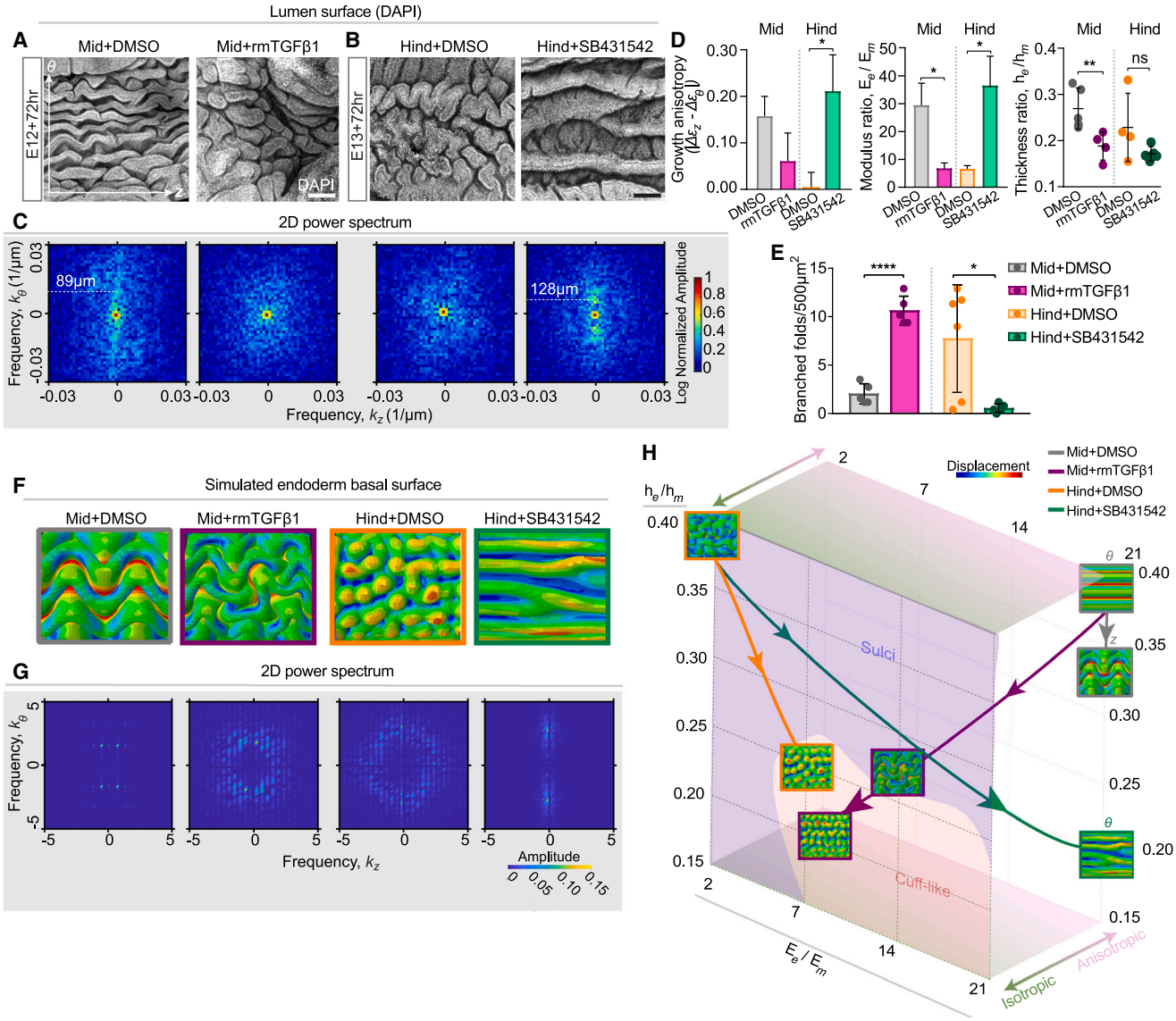


Figure 5. *Ex vivo* perturbations of TGF-β signaling capture midgut and hindgut folding patterns and mechanical properties

(A and B) Lumen surfaces of midgut (A) and hindgut (B) TGF-β perturbations. Scale bars, 100 μm.

(C) Power spectra labeled with characteristic wavelengths on the circumferential axis (Θ).

(D) Growth anisotropy (n = 7–9 gut segments, 4 embryos/condition; see Figure S6G and STAR Methods), modulus ratios (n = 5–8 gut samples, 4 embryos/condition; see Figure S6E), and thickness ratios (n = 4 sections, 2 embryos/ condition) for explant conditions.

(E) Branched folds per 500 μm^2 (n = 4 images, 2–3 embryos/condition).

(F and G) (F) Numerical simulation results for different explant conditions (Table S1) and (G) associated power spectra.

(H) 3D parameter space from Figure 2G with mapped explant trajectories. Initial states correspond to E12 simulations of midgut and hindgut wrinkling. (D) and (E) Unpaired, two-tailed t test. Error bars, SEM. *p < 0.05; **p < 0.01; ****p < 0.0001; ns, not significant.

See also Figure S6 and Table S1.

geometry, stiffness, and differential growth of endoderm and mesenchyme layers. Though properties of the endoderm layer were unaffected (Figures S6C and S6E), both modulus and thickness of the midgut mesenchyme increased with TGF-β activation (Figures S6D and S6F). The resulting lower endoderm-to-mesenchyme modulus and thickness ratios mimic the mechanical properties of the hindgut (Figure 5D).

Suppression of TGF-β signaling also increased the modulus ratio of the hindgut by reducing the mesenchyme modulus but did not alter its thickness ratio (Figures 5D, S6D, and S6F). Therefore, while TGF-β signaling promotes thickening and stiffening of the midgut mesenchyme toward a hindgut-like state, it is not needed to thicken the hindgut mesenchyme. Instead, suppression of the pathway mimics the midgut by dramatically lowering the mesenchyme modulus (Figure S6F).

To evaluate differential growth, we calculated strains at the end of each culture experiment and compared with initial strains at E12 to measure relative growth on each axis (Figure S6G)

Please cite this article in press as: Gill et al., Hox gene activity directs physical forces to differentially shape chick small and large intestinal epithelia, Developmental Cell (2024), https://doi.org/10.1016/j.devcel.2024.07.012

(STAR Methods). We expected that if growth properties are switched between compartments with pathway perturbations, the change in strain will be roughly equal on both axes (isotropic) for the midgut with exogenous TGF-β1 and more pronounced on one axis than the other for the hindgut with TGF-β suppression (anisotropic). Indeed, the TGF-β1-treated midgut experienced relatively similar changes in compression longitudinally and circumferentially (Figure S6G). When endogenous TGF-β was suppressed in the hindgut by SB431542 treatment, however, only circumferential compressive strains increased. Thus, in line with genetic perturbations, growth was closer to anisotropic in the cases resulting in ridge/zigzag morphologies and closer to isotropic when sulci formed (Figure 5D). TGF-β signaling therefore disrupted the anisotropic growth profile characteristic of the midgut, similar to the effects of *HOXD13* misexpression.

Simulated explant morphologies fall along endogenous trajectories in a 3D parameter space

We next asked whether observed differences in mechanical properties in our explant cultures are sufficient to explain their lumen morphologies. We therefore mapped positions of explant morphological trajectories with and without TGF-β perturbations to our 3D parameter space defined in Figure 2G using measured parameters. Trajectories for midgut and hindgut conditions diverge between isotropic and anisotropic planes (Figure 5H), and simulations corresponding to measured explant properties qualitatively and quantitatively match lumen morphologies observed experimentally (compare Figures 5A–5C to 5F and 5G). Our model results therefore indicate that we can, in fact, attribute lumen morphology changes upon TGF-β perturbation to changes in physical and geometric parameters.

Taken together, our data suggest that HOXD13 controls mesenchymal thickness, modulus, and growth orientation (and, hence, gut lumen morphology) through transcriptional changes to genes in the TGF-β pathway. That leaves unexplained, however, how TGF-β signaling alters the physical properties of the gut tissues to achieve this effect.

TGF-β signaling alters mesenchymal geometry and drives lumen morphogenesis through modulation of the ECM

Prominent among the genes differentially expressed in the mesenchyme of both the hindgut and *HOXD13*-expressing midgut at E14 were *COL1A1* and *COL1A2*, encoding the pro-alpha1 and alpha2 chains of collagen 1 (COL1) (Figures 3B and 3C). A change in the extracellular matrix (ECM) would be expected to affect the geometric and material properties of tissues, and TGF-β signaling is known to regulate COL1 production in other settings.[44] We therefore analyzed radial COL1 distributions in immunostained midgut, hindgut, and RCAS-*HOXD13* midgut sections and found that while it is limited to a domain immediately adjacent to circumferential muscle in the midgut (roughly co-localizing with smooth muscle, pSMAD2, and TGF-β gene expression), COL1 extends to the basement membrane in the hindgut and *HOXD13*-expressing midgut, consistent with a possible role in altering properties of the subepithelial mesenchyme, as in other tissues[45] (Figure 6A).

To test whether TGF-β regulates collagen distribution in the developing gut, we first tried culturing the hindgut in the presence of Col003, an Hsp47 inhibitor that prevents secretion of collagen.[46] However, this condition had no effect on lumen morphology or collagen distribution, likely due to pre-existing collagen that is unaffected by halted secretion (Figures S6I and S6J). Therefore, we instead cultured the midgut with both TGF-β1 and the collagen secretion inhibitor. While TGF-β is sufficient to change the midgut luminal morphology to resemble that of the hindgut, the TGF-β + Col003 lumen pattern instead resembled that of the vehicle-treated control midgut (Figures 6C, 6D, S6A, and S6B). TGF-β is thus unable to promote hindgut morphology when collagen deposition is blocked. Accordingly, as with *HOXD13* misexpression in the midgut, TGF-β treated midguts display COL1 extending to the basement membrane, but this localization is lost when collagen secretion is inhibited with Col003 (Figure 6B).

To then determine which of the physical properties of the developing hindgut regulated by TGF-β signaling (downstream of *HOXD13* activity) are dependent on collagen, we examined the material, geometric, and growth properties of the midgut treated with both TGF-β and Col003. Blocking collagen secretion did not affect the increase in mesenchyme modulus seen in the TGF-β treated midguts (Figures 6E and S6F), potentially consistent with the fact that crosslinking of collagen into fibril networks, not deposition alone, is critical to confer tissue stiffness.[47] However, TGF-β-induced mesenchyme thickening (which decreased thickness ratio) was rescued, and growth anisotropy was restored (Figures 6F, S6D, and S6G). This result suggests that deposition of new collagen protein contributes to mesenchyme geometry and that these geometric changes are required for TGF-β signaling to successfully transform the midgut lumen to a hindgut-like morphology.

Finally, we asked which mesenchymal cells are responsible for hindgut-specific ECM remodeling. TGF-β signaling induces differentiation of myofibroblasts, or contractile cells that heavily deposit fibrous matrix proteins and take on qualities of both fibroblasts and muscle cells[48,49]; therefore, one possibility is that the distribution or abundance of myofibroblast or myofibroblast-like mesenchymal subtypes is distinct in the hindgut compared with the midgut. Indeed, scRNA-seq revealed a mesenchymal subpopulation in the hindgut that bridges mesenchyme and muscle cell types and is absent from midgut datasets (Figures S5C, S5D, and S7A). Markers of this cluster include established intestinal fibroblast markers like *GREM1*, *BMPER*, and *RSPO3*, with a subset of cells highly expressing myofibroblast genes like *TAGLN* and *MYL9* (Figures S7B and S7F). Cells in this cluster also express TGF-β pathway-related ECM factors and ligands (Figure S7F).

Concurrently, we used Light-seq spatial RNA-seq[50] (STAR Methods) to identify genes that are commonly differentially expressed in the hindgut and RCAS-*HOXD13* subepithelial mesenchyme alone, where we observed specialized mechanical properties and a higher proportion of pSMAD2+ cells in the hindgut (Figures S7C–S7E). The top hits from this analysis include myofibroblast and ECM-related factors that are established downstream targets of TGF-β pathway activation,[51–55] and that show high expression in the *GREM1*+ *BMPER*+ hindgut subpopulation (Figure S7F). These data suggest a model where increased activation of TGF-β signaling leads to a higher proportion of fibroblasts and myofibroblast-associated cells that

Please cite this article in press as: Gill et al., Hox gene activity directs physical forces to differentially shape chick small and large intestinal epithelia, Developmental Cell (2024), https://doi.org/10.1016/j.devcel.2024.07.012

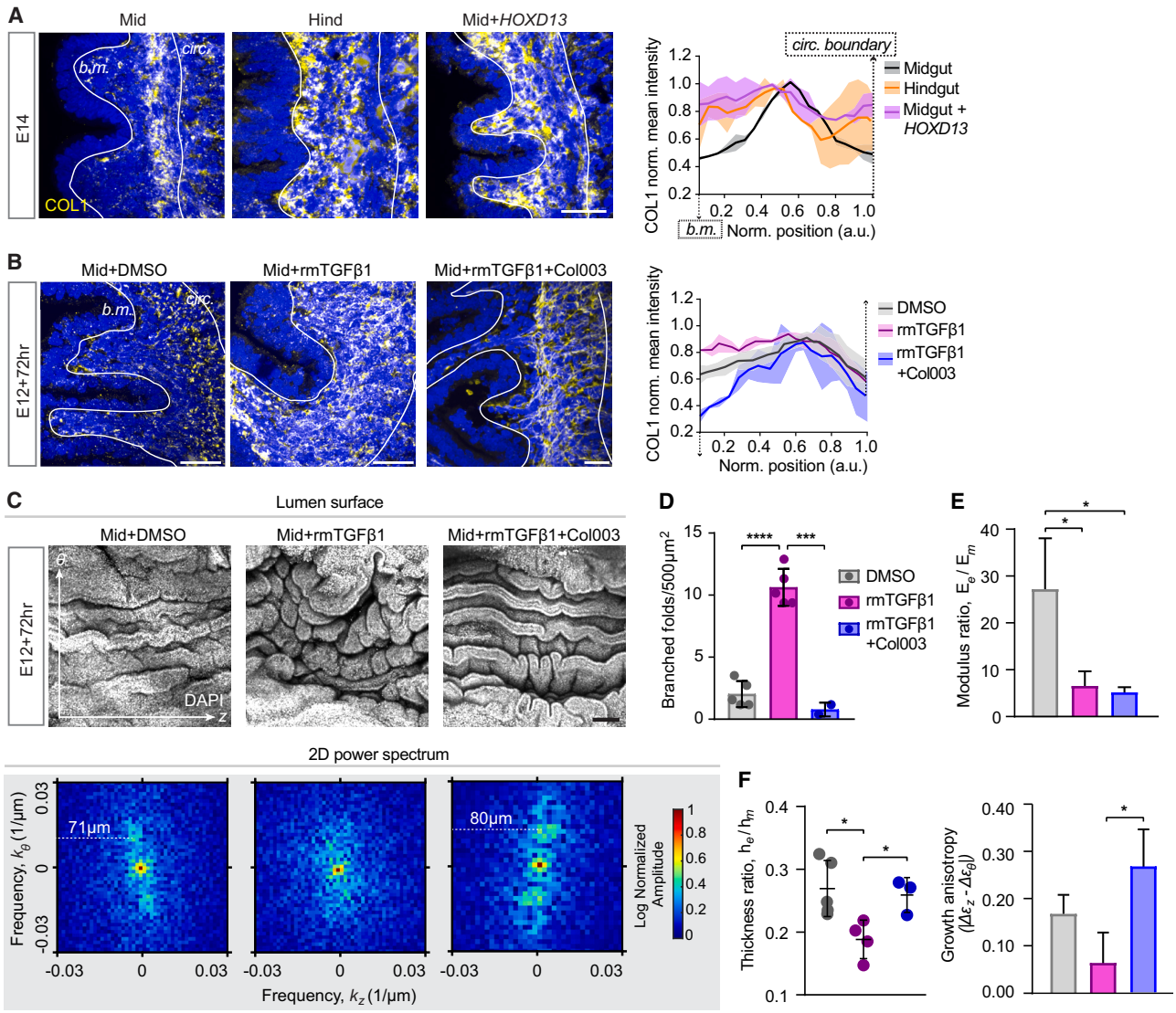


Figure 6. TGF-β-induced extracellular matrix remodeling affects lumen morphology

(A and B) Collagen 1 (COL1) immunostains and corresponding radial intensity profiles for (A) midgut, hindgut, and RCAS-*HOXD13* midgut samples and (B) midgut explant experiments with Col003 treatment (n = 3 sections, 1–2 embryos/condition). b.m., basement membrane; circ., circumferential muscle boundary. Scale bars, 20 μm; shaded area, SD.

(C) Lumen surfaces and power spectra with characteristic wavelengths on the circumferential axis (Θ). Scale bars, 100 μm.

(D–F) (D) Branched folds per 500 μm² (n = 4 images, 2–3 embryos/condition), (E) modulus ratios (n = 6–8 gut segments, 2–4 embryos; see Figures S6E and S6F), and (F) thickness ratios (n = 4 sections, 2 embryos/condition), and growth anisotropy (n = 6–10 gut segments, 4 embryos/condition; see Figure S6G).

(D)–(F) One-way ANOVA, Tukey's MCT. *p < 0.05; ***p < 0.001; ****p < 0.0001.

See also Figure S6.

deposit ECM within the hindgut mesenchyme, thereby affecting mechanical properties and, ultimately, lumen morphology.

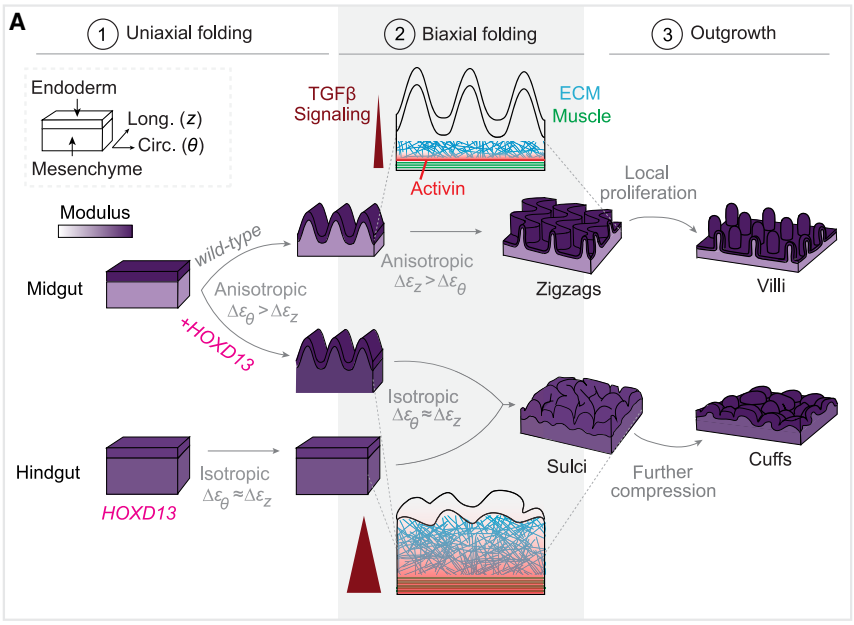
DISCUSSION

A model for the specialization of intestinal luminal morphology integrating genetic and mechanical influences downstream of Hox activity

Both molecular patterning and physical forces cooperate to shape organs, but the phenomena that translate gene expression into forces (and vice versa) have, until recently, remained a mystery.[56–59] In few cases is this more salient than the question of how Hox genes specify appropriate regional forms in the developing embryo.

Prior to our study, genetic evidence had made it clear that Hox and ParaHox gene activity determine regional differences in the developing gut tube and that *Hoxd13*, in particular, plays a key role in specifying hindgut morphology.[12,13] However, how this critical Hox code affected downstream gene expression and cell behavior to alter gut morphogenesis remained unclear. The

Please cite this article in press as: Gill et al., Hox gene activity directs physical forces to differentially shape chick small and large intestinal epithelia, Developmental Cell (2024), https://doi.org/10.1016/j.devcel.2024.07.012



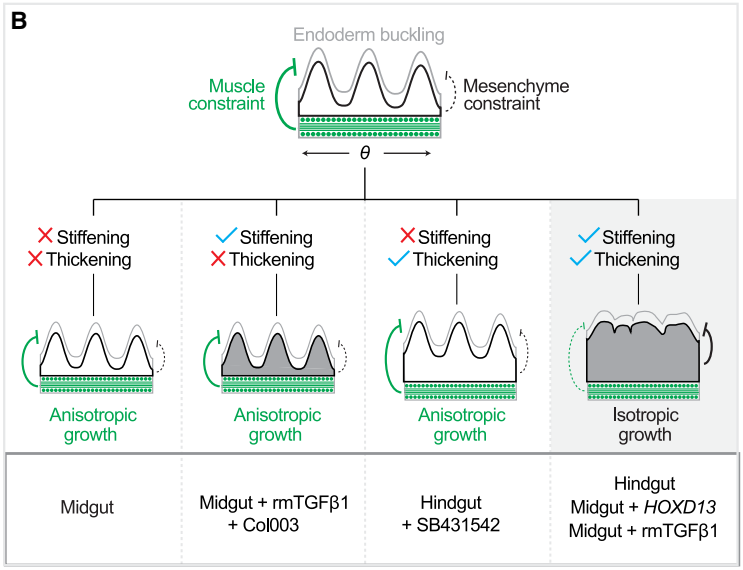


Figure 7. A genetic and mechanical model of differential intestinal morphogenesis in the chick

(A) Summary of the integration of physical forces, signaling, and extracellular matrix (ECM) remodeling that guides hindgut lumen morphogenesis downstream of HOXD13 activity, shown in 3 stages. Enlarged longitudinal view during stage 2 highlights regional ECM, muscle, and Activin A/TGF-β signaling patterns.

(B) Perturbation effects on morphology, tissue geometry, stiffness, and growth. Dashed curve indicating inhibition, minimal constraint; thick curve, predominant constraint; gray shading in the mesenchyme, stiffening. rmTGFβ1, recombinant mouse TGFβ1.

data presented here allows us to propose a model that bridges Hox patterning to the physical forces that govern morphogenesis (Figure 7A).

Mechanical perturbations lend insight into how the endoderm negotiates muscular vs. mesenchymal constraint

Our findings provide insight into why the hindgut lumen fails to undergo stepwise buckling despite stepwise muscle differentiation. In the wild-type midgut, the endoderm undergoes anisotropic growth due to constraint imposed by smooth muscle layers—from a mechanical standpoint, the mesenchyme is simply a thin and soft intermediary (Figure 7B). However, stiffening and thickening of the mesenchyme increases its bending stiffness and resistance to deformation, thus decreasing the role of muscle in dictating endoderm buckling. We therefore propose that the endoderm buckles simultaneously on both axes to form sulci because it is subject to constraint from the stiffer and thicker mesenchyme layer, preempting the constraint from highly oriented muscle[26] (Figure 7B). Furthermore, as evidenced by the hindgut treated with SB431542 and the midgut treated with TGF-β and Col003, neither thickening nor stiffening alone is sufficient to overcome muscle constraint on endoderm growth to confer sulci and cuffs.

Functional implications of differential morphogenesis in the small and large intestines

Although descriptions of the colonic epithelium have largely focused on its lack of villi and Paneth cells (with an increase in goblet cells), the appearance of superficial, branched, and striated folds like those we have described here is a common feature across birds and mammals, including humans.[60,61] Since high epithelial curvature concentrates mesenchymal morphogen signals in the chick to pattern the chick crypt-villus axis,[62] the mechanical context that generates sulci and maintains a flat hindgut epithelial-mesenchymal interface precludes the morphogen distributions that define villi and differentiated cells found in the small intestine. Along with the previous finding that *HOXD13* misexpression induces differentiation of cell types found in the hindgut,[19] our results suggest that the topographical consequence of regional mechanics may contribute to functional differences between intestinal compartments.

An instructive role of HOXD13 in hindgut morphogenesis

Formative work on Hox patterning in the mouse intestine pinpointed *Hoxd13* mutant phenotypes to the terminal anorectal region.[12,17] However, expression of *HFGa13* (a dominant negative form of HOXA13) in the chick hindgut endoderm affects development of the entire hindgut caudal to the ceca.[15] Given that *HOXA13* and *HOXD13* mutants generally show similar

Please cite this article in press as: Gill et al., Hox gene activity directs physical forces to differentially shape chick small and large intestinal epithelia, Developmental Cell (2024), https://doi.org/10.1016/j.devcel.2024.07.012

phenotypes, especially for overexpression in the chick, it appears that Hox group 13 gene expression in the hindgut affects both the formation of the caudal gut more broadly and later morphogenesis of the luminal lining. Other Hox and ParaHox genes have also been implicated in hindgut development, such as *Cdx2* and *Hoxd12*.[18,63–67] Whether the mechanisms downstream of these genes regulate physical properties to promote posterior identity is not known and could be a subject of future study.

TGF-β regulation of ECM during gut development

Besides its essential function in regulating the gut immune system, TGF-β has primarily been implicated in intestinal fibrosis, which is marked by excessive tissue thickening and stiffening via changes to cell and ECM properties.[44,68] TGF-β signaling upregulation in fibrotic conditions leads to differentiation or transdifferentiation of mesenchymal cell types into myofibroblasts.[48,49]

As in the case of fibrosis, we find that TGF-β signaling modulates tissue thickening and stiffening during normal gut development by regulating ECM remodeling. We report the presence of a mesenchymal subpopulation in the hindgut that highly expresses the same markers as cells that affect ECM organization in the colon (trophocytes),[69,70] cells involved in intestinal supramolecular ECM fiber organization (S3 fibroblasts),[69,71,72] as well as myofibroblastic cancer-associated fibroblasts.[73,74] Additionally, during mouse development, TGF-β-mediated differentiation of myofibroblasts shortens the developing mouse midgut, suggesting that proper regulation of this pathway is indeed needed for regional gut shaping.[75]

Limitations of the study

Both this study and our prior study of midgut lumen morphogenesis relied on *in silico* models; together, they lend insight into the relative importance of local (cell-scale) and global (tissue- and organ-scale) morphogenetic phenomena in intestinal development and evolution.[25,26] However, we have thus far treated gut tissues as elastic solids without considering additional material properties of deforming layers that may also be relevant, such as fluid properties, which have been shown to be involved in intestinal lumen morphogenesis[59] and would influence how the lumen deforms on long vs. short timescales. Future studies could parse contributions of different material properties with the aid of physical models to precisely control biophysical parameters. Additionally, local heterogeneity in stiffness, growth, and thickness, which we did not consider here, may also help explain regional differences in lumen morphology.

STAR★METHODS

Detailed methods are provided in the online version of this paper and include the following:

- KEY RESOURCES TABLE
- RESOURCE AVAILABILITY
  - Lead contact
  - Materials availability
  - Data and code availability
- EXPERIMENTAL MODEL AND STUDY PARTICIPANT DETAILS
  - Chickens
- METHOD DETAILS
  - Plasmids
  - Chick intestinal electroporation
  - Sparse, inducible HOXD13 expression
  - Lumen surface imaging
  - Surface wrinkling quantification
  - Fold aspect ratio quantification
  - Section immunostaining and quantification
  - Fluorescence in situ hybridization
  - Mechanical measurements
  - Bulk RNA sequencing
  - Single cell RNA sequencing
  - Chick intestinal explant culture
  - Light-seq spatial RNA sequencing
  - Numerical simulations
- QUANTIFICATION AND STATISTICAL ANALYSIS

SUPPLEMENTAL INFORMATION

Supplemental information can be found online at https://doi.org/10.1016/j.devcel.2024.07.012.

ACKNOWLEDGMENTS

We thank members of the Tabin, Cepko, and Nerurkar labs for helpful discussions, as well as Emma R. West and Ninning Liu for assistance with Light-seq data collection and analysis. We acknowledge financial support from NSF-ANR grant 2204058 (S.Y. and L.M.), the NIH (L.M.), the Simons Foundation (L.M.), the Henri Seydoux Fund (L.M.), and NIH award 5RO1HD087234 (C.J.T.). Portions of this paper were developed from the thesis of H.K.G.

AUTHOR CONTRIBUTIONS

H.K.G. and C.J.T. conceived of the study; H.K.G. collected and analyzed experimental data with contributions from J.C.L. and C.L.; S.Y. developed the theoretical model and performed numerical simulations with contributions from H.K.G., under guidance from L.M.; H.K.G., J.C.L., N.L.N., C.L., and T.R.H. devised methodologies for experiments and data analysis; H.K.G. and C.J.T. wrote the manuscript with contributions from S.Y.; L.M., T.R.H., J.C.L., N.L.N., and C.L. contributed feedback for edits; and C.J.T. and L.M. supervised the study.

DECLARATION OF INTERESTS

The authors declare no competing interests.

Received: June 21, 2023
Revised: April 15, 2024
Accepted: July 11, 2024
Published: August 7, 2024

REFERENCES

1. Lewis, E.B. (1963). Genes and developmental pathways. Am. Zool. *3*, 33–56. https://doi.org/10.1093/icb/3.1.33.
2. Lewis, E.B. (1978). A gene complex controlling segmentation in Drosophila. Nature *276*, 565–570. https://doi.org/10.1038/276565A0.
3. McGinnis, W., Levine, M.S., Hafen, E., Kuroiwa, A., and Gehring, W.J. (1984). A conserved DNA sequence in homoeotic genes of the Drosophila Antennapedia and bithorax complexes. Nature *308*, 428–433. https://doi.org/10.1038/308428A0.
4. Scott, M.P., and Weiner, A.J. (1984). Structural relationships among genes that control development: sequence homology between the Antennapedia, Ultrabithorax, and fushi tarazu loci of Drosophila. Proc. Natl. Acad. Sci. USA *81*, 4115–4119. https://doi.org/10.1073/PNAS.81.13.4115.
5. Carrasco, A.E., McGinnis, W., Gehring, W.J., and de Robertis, E.M. (1984). Cloning of an X. laevis gene expressed during early embryogenesis coding for a peptide region homologous to Drosophila homeotic genes. Cell *37*, 409–414. https://doi.org/10.1016/0092-8674(84)90371-4.

Please cite this article in press as: Gill et al., Hox gene activity directs physical forces to differentially shape chick small and large intestinal epithelia, Developmental Cell (2024), https://doi.org/10.1016/j.devcel.2024.07.012

6. McGinnis, W., Garber, R.L., Wirz, J., Kuroiwa, A., and Gehring, W.J. (1984). A homologous protein-coding sequence in Drosophila homeotic genes and its conservation in other metazoans. Cell *37*, 403–408. https://doi.org/10.1016/0092-8674(84)90370-2.

7. Kessel, M., and Gruss, P. (1991). Homeotic Transformations of Murine Vertebrae and Concomitant Alteration of Hox Codes Induced by Retinoic Acid. Cell *67*, 89–104. https://doi.org/10.1016/0092-8674(91)90574-i.

8. Wellik, D.M. (2007). Hox patterning of the vertebrate axial skeleton. Dev. Dyn. *236*, 2454–2463. https://doi.org/10.1002/dvdy.21286.

9. De Las Heras, J.M., García-Cortés, C., Foronda, D., Pastor-Pareja, J.C., Shashidhara, L.S., and Sánchez-Herrero, E. (2018). The Drosophila Hox gene Ultrabithorax controls appendage shape by regulating extracellular matrix dynamics. Development *145*, 1–10. https://doi.org/10.1242/dev.161844.

10. Mitchell, N.P., Cislo, D.J., Shankar, S., Lin, Y., Shraiman, B.I., and Streichan, S.J. (2022). Visceral organ morphogenesis via calcium-patterned muscle constrictions. eLife *11*, e77355. https://doi.org/10.7554/eLife.77355.

11. Annunziata, R., Andrikou, C., Perillo, M., Cuomo, C., and Arnone, M.I. (2019). Development and evolution of gut structures: from molecules to function. Cell Tissue Res. *377*, 445–458. https://doi.org/10.1007/s00441-019-03093-9.

12. Kondo, T., Dollé, P., Zákány, J., and Duboule, D. (1996). Function of posterior HoxD genes in the morphogenesis of the anal sphincter. Development *122*, 2651–2659. https://doi.org/10.1242/dev.122.9.2651.

13. Roberts, D.J., Johnson, R.L., Burke, A.C., Nelson, C.E., Morgan, B.A., and Tabin, C. (1995). Sonic hedgehog is an endodermal signal inducing Bmp-4 and Hox genes during induction and regionalization of the chick hindgut. Development *121*, 3163–3174. https://doi.org/10.1242/dev.121.10.3163.

14. Yokouchi, Y., Sakiyama, J.I., and Kuroiwa, A. (1995). Coordinated expression of Abd-B subfamily genes of the HoxA cluster in the developing digestive tract of chick embryo. Dev. Biol. *169*, 76–89. https://doi.org/10.1006/dbio.1995.1128.

15. De Santa Barbara, P., and Roberts, D.J. (2002). Tail gut endoderm and gut/genitourinary/tail development: a new tissue- specific role for Hoxa13. Development *129*, 551–561. https://doi.org/10.1242/dev.129.3.551.

16. Dan, Z., Bo, Z.Z., Tao, Z., Wei, Z.S., Jia, W.D., Cheng, Z.S., Wei, Y.Z., and Wang, W.L. (2010). Hoxd-13 expression in the development of hindgut in ethylenethiourea-exposed fetal rats. J. Pediatr. Surg. *45*, 755–761. https://doi.org/10.1016/j.jpedsurg.2009.11.011.

17. Warot, X., Fromental-Ramain, C., Fraulob, V., Chambon, P., and Dollé, P. (1997). Gene dosage-dependent effects of the Hoxa-13 and Hoxd-13 mutations on morphogenesis of the terminal parts of the digestive and urogenital tracts. Development *124*, 4781–4791. https://doi.org/10.1242/dev.124.23.4781.

18. Zákány, J., and Duboule, D. (1999). Hox genes and the making of sphincters. Nature *401*, 761–762. https://doi.org/10.1038/44511.

19. Roberts, D.J., Smith, D.M., Goff, D.J., and Tabin, C.J. (1998). Epithelial-mesenchymal signaling during the regionalization of the chick gut. Development *125*, 2791–2801. https://doi.org/10.1242/dev.125.15.2791.

20. Bell, L., and Williams, L. (1982). A scanning and transmission electron microscopical study of the morphogenesis of human colonic villi. Anat. Embryol. (Berl) *165*, 437–455. https://doi.org/10.1007/BF00305579.

21. De Santa Barbara, P., Van Den Brink, G.R., and Roberts, D.J. (2003). Development and differentiation of the intestinal epithelium. Cell. Mol. Life Sci. *60*, 1322–1332. https://doi.org/10.1007/s00018-003-2289-3.

22. Mahoney, Z.X., Stappenbeck, T.S., and Miner, J.H. (2008). Laminin α5 influences the architecture of the mouse small intestine mucosa. J. Cell Sci. *121*, 2493–2502. https://doi.org/10.1242/jcs.025528.

23. Helander, H.F. (1973). Morphological studies on the development of the rat colonic mucosa. Acta Anat. *85*, 155–176. https://doi.org/10.1159/000143991.

24. Spence, J.R., Lauf, R., and Shroyer, N.F. (2011). Vertebrate intestinal endoderm development. Dev. Dyn. *240*, 501–520. https://doi.org/10.1002/dvdy.22540.

25. Shyer, A.E., Tallinen, T., Nerurkar, N.L., Wei, Z., Gil, E.S., Kaplan, D.L., Tabin, C.J., and Mahadevan, L. (2013). Villification: How the gut gets its villi. Science *342*, 212–218. https://doi.org/10.1126/science.1238842.

26. Gill, H.K., Yin, S., Lawlor, J.C., Huycke, T.R., Nerurkar, N.L., Tabin, C.J., and Mahadevan, L. (2024). The developmental mechanics of divergent buckling patterns in the chick gut. Proc. Natl. Acad. Sci. USA *121*, e2310992121. https://doi.org/10.1073/pnas.2310992121.

27. Coulombre, A.J., and Coulombre, J.L. (1958). Intestinal development. I. Morphogenesis of the villi and musculature. J. Embryol. Exp. Morphol. *6*, 403–411. https://doi.org/10.1242/dev.6.3.403.

28. Hohlfeld, E., and Mahadevan, L. (2011). Unfolding the sulcus. Phys. Rev. Lett. *106*, 105702. https://doi.org/10.1103/PhysRevLett.106.105702.

29. Hohlfeld, E., and Mahadevan, L. (2012). Scale and nature of sulcification patterns. Phys. Rev. Lett. *109*, 025701. https://doi.org/10.1103/PhysRevLett.109.025701.

30. Tallinen, T., Biggins, J.S., and Mahadevan, L. (2013). Surface sulci in squeezed soft solids. Phys. Rev. Lett. *110*, 024302. https://doi.org/10.1103/PhysRevLett.110.024302.

31. Ciarletta, P., Balbi, V., and Kuhl, E. (2014). Pattern selection in growing tubular tissues. Phys. Rev. Lett. *113*, 248101. https://doi.org/10.1103/PhysRevLett.113.248101.

32. Holland, M., Budday, S., Goriely, A., and Kuhl, E. (2018). Symmetry Breaking in Wrinkling Patterns: Gyri Are Universally Thicker than Sulci. Phys. Rev. Lett. *121*, 228002. https://doi.org/10.1103/PhysRevLett.121.228002.

33. Razavi, M.J., Pidaparti, R., and Wang, X. (2016). Surface and interfacial creases in a bilayer tubular soft tissue. Phys. Rev. E *94*, 022405. https://doi.org/10.1103/PhysRevE.94.022405.

34. Tallinen, T., Chung, J.Y., Biggins, J.S., and Mahadevan, L. (2014). Gyrification from constrained cortical expansion. Proc. Natl. Acad. Sci. USA *111*, 12667–12672. https://doi.org/10.1073/pnas.1406015111.

35. Tallinen, T., and Biggins, J.S. (2015). Mechanics of invagination and folding: Hybridized instabilities when one soft tissue grows on another. Phys. Rev. E Stat. Nonlin. Soft Matter Phys. *92*, 022720. https://doi.org/10.1103/PhysRevE.92.022720.

36. Ben Amar, M., and Jia, F. (2013). Anisotropic growth shapes intestinal tissues during embryogenesis. Proc. Natl. Acad. Sci. USA *110*, 10525–10530. https://doi.org/10.1073/pnas.1217391110.

37. Huycke, T.R., Miller, B.M., Gill, H.K., Nerurkar, N.L., Sprinzak, D., and Mahadevan, L. (2019). Genetic and Mechanical Regulation of Intestinal Smooth Muscle Development. Cell *179*, 90–105.e21. https://doi.org/10.1016/j.cell.2019.08.041.

38. Derynck, R., and Budi, E.H. (2019). Specificity, versatility, and control of TGF-β family signaling. Sci. Signal. *12*, eaav5183. https://doi.org/10.1126/scisignal.aav5183.

39. Gurdziel, K., Vogt, K.R., Schneider, G., Richards, N., and Gumucio, D.L. (2016). Computational prediction and experimental validation of novel Hedgehog-responsive enhancers linked to genes of the Hedgehog pathway. BMC Dev. Biol. *16*, 4. https://doi.org/10.1186/s12861-016-0106-0.

40. Havis, E., Bonnin, M.A., Esteves de Lima, J., Charvet, B., Milet, C., and Duprez, D. (2016). TGFβ and FGF promote tendon progenitor fate and act downstream of muscle contraction to regulate tendon differentiation during chick limb development. Development *143*, 3839–3851. https://doi.org/10.1242/dev.136242.

41. Tzavlaki, K., and Moustakas, A. (2020). TGF-β Signaling. Biomolecules *10*, 487. https://doi.org/10.3390/biom10030487.

Please cite this article in press as: Gill et al., Hox gene activity directs physical forces to differentially shape chick small and large intestinal epithelia, Developmental Cell (2024), https://doi.org/10.1016/j.devcel.2024.07.012

42. Wang, C., Liu, P., Wu, H., Cui, P., Li, Y., Liu, Y., Liu, Z., and Gou, S. (2016). MicroRNA-323-3p inhibits cell invasion and metastasis in pancreatic ductal adenocarcinoma via direct suppression of SMAD2 and SMAD3. Oncotarget *7*, 14912–14924. https://doi.org/10.18632/oncotarget.7482.

43. McCarthy, N., Tie, G., Madha, S., He, R., Kraiczy, J., Maglieri, A., and Shivdasani, R.A. (2023). Smooth muscle contributes to the development and function of a layered intestinal stem cell niche. Dev. Cell *58*, 550–564.e6. https://doi.org/10.1016/j.devcel.2023.02.012.

44. Verrecchia, F., and Mauviel, A. (2002). Transforming growth factor-β signaling through the Smad pathway: Role in extracellular matrix gene expression and regulation. J. Invest. Dermatol. *118*, 211–215. https://doi.org/10.1046/j.1523-1747.2002.01641.x.

45. Rozario, T., and DeSimone, D.W. (2010). The extracellular matrix in development and morphogenesis: A dynamic view. Dev. Biol. *341*, 126–140. https://doi.org/10.1016/j.ydbio.2009.10.026.

46. Wu, S., Liang, C., Xie, X., Huang, H., Fu, J., Wang, C., Su, Z., Wang, Y., Qu, X., Li, J., et al. (2021). Hsp47 Inhibitor Col003 Attenuates Collagen-Induced Platelet Activation and Cerebral Ischemic-Reperfusion Injury in Rats. Front. Pharmacol. *12*, 792263. https://doi.org/10.3389/fphar.2021.792263.

47. Brereton, C.J., Yao, L., Davies, E.R., Zhou, Y., Vukmirovic, M., Bell, J.A., Wang, S., Ridley, R.A., Dean, L.S.N., Andriotis, O.G., et al. (2022). Pseudohypoxic HIF pathway activation dysregulates collagen structure-function in human lung fibrosis. eLife *11*, e69348. https://doi.org/10.7554/eLife.69348.

48. Stolfi, C., Troncone, E., Marafini, I., and Monteleone, G. (2020). Role of tgf-beta and smad7 in gut inflammation, fibrosis and cancer. Biomolecules *11*, 1–15. https://doi.org/10.3390/biom11010017.

49. Vallée, A., and Lecarpentier, Y. (2019). TGF-β in fibrosis by acting as a conductor for contractile properties of myofibroblasts. Cell Biosci. *9*, 98. https://doi.org/10.1186/s13578-019-0362-3.

50. Kishi, J.Y., Liu, N., West, E.R., Sheng, K., Jordanides, J.J., Serrata, M., Cepko, C.L., Saka, S.K., and Yin, P. (2022). Light-Seq: light-directed in situ barcoding of biomolecules in fixed cells and tissues for spatially indexed sequencing. Nat. Methods *19*, 1393–1402. https://doi.org/10.1038/s41592-022-01604-1.

51. Aldeiri, B., Roostalu, U., Albertini, A., Wong, J., Morabito, A., and Cossu, G. (2017). Transgelin-expressing myofibroblasts orchestrate ventral midline closure through TGFβ signalling. Development *144*, 3336–3348. https://doi.org/10.1242/dev.152843.

52. Guerrero-Juarez, C.F., Dedhia, P.H., Jin, S., Ruiz-Vega, R., Ma, D., Liu, Y., Yamaga, K., Shestova, O., Gay, D.L., Yang, Z., et al. (2019). Single-cell analysis reveals fibroblast heterogeneity and myeloid-derived adipocyte progenitors in murine skin wounds. Nat. Commun. *10*, 650. https://doi.org/10.1038/s41467-018-08247-x.

53. Klingberg, F., Hinz, B., and White, E.S. (2013). The myofibroblast matrix: implications for tissue repair and fibrosis. J. Pathol. *229*, 298–309. https://doi.org/10.1002/PATH.4104.

54. Liu, G., Cooley, M.A., Jarnicki, A.G., Borghuis, T., Nair, P.M., Tjin, G., Hsu, A.C., Haw, T.J., Fricker, M., Harrison, C.L., et al. (2019). Fibulin-1c regulates transforming growth factor–β activation in pulmonary tissue fibrosis. JCI Insight *5*, e124529. https://doi.org/10.1172/JCI.INSIGHT.124529.

55. Hattori, N., Carrino, D.A., Lauer, M.E., Vasanji, A., Wylie, J.D., Nelson, C.M., and Apte, S.S. (2011). Pericellular versican regulates the fibroblast-myofibroblast transition: a role for ADAMTS5 protease-mediated proteolysis. J. Biol. Chem. *286*, 34298–34310. https://doi.org/10.1074/jbc.M111.254938.

56. De Belly, H., Paluch, E.K., and Chalut, K.J. (2022). Interplay between mechanics and signalling in regulating cell fate. Nat. Rev. Mol. Cell Biol. *23*, 465–480. https://doi.org/10.1038/s41580-022-00472-z.

57. Hallou, A., and Brunet, T. (2020). On growth and force: mechanical forces in development. Development *147*, dev187302. https://doi.org/10.1242/dev.187302.

58. LeGoff, L., and Lecuit, T. (2015). Mechanical forces and growth in animal tissues. Cold Spring Harb. Perspect. Biol. *8*, a019232. https://doi.org/10.1101/cshperspect.a019232.

59. Huycke, T.R., Häkkinen, T.J., Miyazaki, H., Srivastava, V., Barruet, E., McGinnis, C.S., Kalantari, A., Cornwall-Scoones, J., Vaka, D., Zhu, Q., et al. (2024). Patterning and folding of intestinal villi by active mesenchymal dewetting. Cell *187*, 3072–3089.e20. https://doi.org/10.1016/j.cell.2024.04.039.

60. Chang, W.W.L., and Leblond, C.P. (1971). Renewal of the epithelium in the descending colon of the mouse. II. Renewal of argentaffin cells. Am. J. Anat. *131*, 101–109. https://doi.org/10.1002/aja.1001310106.

61. Rubio, C.A. (2020). Innominate grooves of the colon: Histological reappraisal. Anticancer Res. *40*, 7031–7035. https://doi.org/10.21873/anticanres.14729.

62. Shyer, A.E., Huycke, T.R., Lee, C., Mahadevan, L., and Tabin, C.J. (2015). Bending Gradients: How the intestinal stem cell gets its home. Cell *161*, 569–580. https://doi.org/10.1016/j.cell.2015.03.041.

63. Gao, N., White, P., and Kaestner, K.H. (2009). Establishment of Intestinal Identity and Epithelial-Mesenchymal Signaling by Cdx2. Dev. Cell *16*, 588–599. https://doi.org/10.1016/j.devcel.2009.02.010.

64. Pinto, R., Barros, R., Pereira-Castro, I., Mesquita, P., da Costa, L.T., Bennett, E.P., Almeida, R., and David, L. (2015). CDX2 homeoprotein is involved in the regulation of ST6GalNAc-I gene in intestinal metaplasia. Lab. Invest. *95*, 718–727. https://doi.org/10.1038/labinvest.2015.52.

65. Silberg, D.G., Sullivan, J., Kang, E., Swain, G.P., Moffett, J., Sund, N.J., Sackett, S.D., and Kaestner, K.H. (2002). Cdx2 ectopic expression induces gastric intestinal metaplasia in transgenic mice. Gastroenterology *122*, 689–696. https://doi.org/10.1053/gast.2002.31902.

66. Sherwood, R.I., Maehr, R., Mazzoni, E.O., and Melton, D.A. (2011). Wnt signaling specifies and patterns intestinal endoderm. Mech. Dev. *128*, 387–400. https://doi.org/10.1016/j.mod.2011.07.005.

67. Zacchetti, G., Duboule, D., and Zakany, J. (2007). Hox gene function in vertebrate gut morphogenesis: The case of the caecum. Development *134*, 3967–3973. https://doi.org/10.1242/dev.010991.

68. Frangogiannis, N.G. (2020). Transforming growth factor–β in tissue fibrosis. J. Exp. Med. *217*, e20190103. https://doi.org/10.1084/jem.20190103.

69. McCarthy, N., Kraiczy, J., and Shivdasani, R.A. (2020). Cellular and molecular architecture of the intestinal stem cell niche. Nat. Cell Biol. *22*, 1033–1041. https://doi.org/10.1038/s41556-020-0567-z.

70. Pærregaard, S.I., Wulff, L., Schussek, S., Niss, K., Mörbe, U., Jendholm, J., Wendland, K., Andrusaite, A.T., Brulois, K.F., Nibbs, R.J.B., et al. (2023). The small and large intestine contain related mesenchymal subsets that derive from embryonic Gli1+ precursors. Nat. Commun. *14*, 2307. https://doi.org/10.1038/s41467-023-37952-5.

71. Kinchen, J., Chen, H.H., Parikh, K., Antanaviciute, A., Jagielowicz, M., Fawkner-Corbett, D., Ashley, N., Cubitt, L., Mellado-Gomez, E., Attar, M., et al. (2018). Structural Remodeling of the Human Colonic Mesenchyme in Inflammatory Bowel Disease. Cell *175*, 372–386.e17. https://doi.org/10.1016/j.cell.2018.08.067.

72. Fawkner-Corbett, D., Antanaviciute, A., Parikh, K., Jagielowicz, M., Gerós, A.S., Gupta, T., Ashley, N., Khamis, D., Fowler, D., Morrissey, E., et al. (2021). Spatiotemporal analysis of human intestinal development at single-cell resolution. Cell *184*, 810–826.e23. https://doi.org/10.1016/j.cell.2020.12.016.

73. Brügger, M.D., and Basler, K. (2023). The diverse nature of intestinal fibroblasts in development, homeostasis, and disease. Trends Cell Biol. *33*, 834–849. https://doi.org/10.1016/j.tcb.2023.03.007.

74. Bauer, J., Emon, M.A.B., Staudacher, J.J., Thomas, A.L., Zessner-Spitzenberg, J., Mancinelli, G., Krett, N., Saif, M.T., and Jung, B. (2020). Increased stiffness of the tumor microenvironment in colon cancer stimulates cancer associated fibroblast-mediated prometastatic activin A signaling. Sci. Rep. *10*, 50. https://doi.org/10.1038/s41598-019-55687-6.

Please cite this article in press as: Gill et al., Hox gene activity directs physical forces to differentially shape chick small and large intestinal epithelia, Developmental Cell (2024), https://doi.org/10.1016/j.devcel.2024.07.012

75. Geske, M.J., Zhang, X., Patel, K.K., Ornitz, D.M., and Stappenbeck, T.S. (2008). Fgf9 signaling regulates small intestinal elongation and mesenchymal development. Development *135*, 2959–2968. https://doi.org/10.1242/dev.020453.

76. Hamburger, V., and Hamilton, H.L. (1992). A series of normal stages in the development of the chick embryo. Dev. Dyn. *195*, 231–272. https://doi.org/10.1002/aja.1001950404.

77. Kan, A., Ikeda, T., Fukai, A., Nakagawa, T., Nakamura, K., Chung, U.I., Kawaguchi, H., and Tabin, C.J. (2013). SOX11 contributes to the regulation of GDF5 in joint maintenance. BMC Dev. Biol. *13*, 4. https://doi.org/10.1186/1471-213X-13-4.

78. Abzhanov, A., Protas, M., Grant, B.R., Grant, P.R., and Tabin, C.J. (2004). Bmp4 and morphological variation of beaks in Darwin's finches. Science *305*, 1462–1465. https://doi.org/10.1126/science.1098095.

79. Nerurkar, N.L., Mahadevan, L., and Tabin, C.J. (2017). BMP signaling controls buckling forces to modulate looping morphogenesis of the gut. Proc. Natl. Acad. Sci. USA *114*, 2277–2282. https://doi.org/10.1073/pnas.1700307114.

80. Chu, D., Nguyen, A., Smith, S.S., Vavrušová, Z., and Schneider, R.A. (2020). Stable integration of an optimized inducible promoter system enables spatiotemporal control of gene expression throughout avian development. Biol. Open *9*, bio055343. https://doi.org/10.1242/bio.055343.

81. Jacko, M., Weyn-Vanhentenryck, S.M., Smerdon, J.W., Yan, R., Feng, H., Williams, D.J., Pai, J., Xu, K., Wichterle, H., and Zhang, C. (2018). Rbfox Splicing Factors Promote Neuronal Maturation and Axon Initial Segment Assembly. Neuron *97*, 853–868.e6. https://doi.org/10.1016/j.neuron.2018.01.020.

82. Choi, H.M.T., Schwarzkopf, M., Fornace, M.E., Acharya, A., Artavanis, G., Stegmaier, J., Cunha, A., and Pierce, N.A. (2018). Third-generation in situ hybridization chain reaction: multiplexed, quantitative, sensitive, versatile, robust. Development *145*, dev165753. https://doi.org/10.1242/dev.165753.

83. Fung, Y.C., and Liu, S.Q. (1989). Change of residual strains in arteries due to hypertrophy caused by aortic constriction. Circ. Res. *65*, 1340–1349. https://doi.org/10.1161/01.RES.65.5.1340.

84. Zhao, J., Chen, X., Yang, J., Liao, D., and Gregersen, H. (2007). Opening angle and residual strain in a three-layered model of pig oesophagus. J. Biomech. *40*, 3187–3192. https://doi.org/10.1016/j.jbiomech.2007.04.002.

85. Love, M.I., Huber, W., and Anders, S. (2014). Moderated estimation of fold change and dispersion for RNA-seq data with DESeq2. Genome Biol. *15*, 550. https://doi.org/10.1186/s13059-014-0550-8.

86. Patro, R., Duggal, G., Love, M.I., Irizarry, R.A., and Kingsford, C. (2017). Salmon provides fast and bias-aware quantification of transcript expression. Nat. Methods *14*, 417–419. https://doi.org/10.1038/nmeth.4197.

87. Chen, E.Y., Tan, C.M., Kou, Y., Duan, Q., Wang, Z., Meirelles, G.V., Clark, N.R., and Ma'ayan, A. (2013). Enrichr: Interactive and collaborative HTML5 gene list enrichment analysis tool. BMC Bioinformatics *14*, 128. https://doi.org/10.1186/1471-2105-14-128.

88. Kuleshov, M.V., Jones, M.R., Rouillard, A.D., Fernandez, N.F., Duan, Q., Wang, Z., Koplev, S., Jenkins, S.L., Jagodnik, K.M., Lachmann, A., et al. (2016). Enrichr: a comprehensive gene set enrichment analysis web server 2016 update. Nucleic Acids Res. *44*, W90–W97. https://doi.org/10.1093/nar/gkw377.

89. Xie, Z., Bailey, A., Kuleshov, M.V., Clarke, D.J.B., Evangelista, J.E., Jenkins, S.L., Lachmann, A., Wojciechowicz, M.L., Kropiwnicki, E., Jagodnik, K.M., et al. (2021). Gene Set Knowledge Discovery with Enrichr. Curr. Protoc. *1*, e90. https://doi.org/10.1002/cpz1.90.

90. Watanabe, M., Kenmotsu, H., Ko, R., Wakuda, K., Ono, A., Imai, H., Taira, T., Naito, T., Murakami, H., Abe, M., et al. (2018). Isolation and molecular analysis of circulating tumor cells from lung cancer patients using a microfluidic chip type cell sorter. Cancer Sci. *109*, 2539–2548. https://doi.org/10.1111/cas.13692.

91. McGinnis, C.S., Patterson, D.M., Winkler, J., Conrad, D.N., Hein, M.Y., Srivastava, V., Hu, J.L., Murrow, L.M., Weissman, J.S., Werb, Z., et al. (2019). MULTI-seq: sample multiplexing for single-cell RNA sequencing using lipid-tagged indices. Nat. Methods *16*, 619–626. https://doi.org/10.1038/s41592-019-0433-8.

92. Huang, Y., McCarthy, D.J., and Stegle, O. (2019). Vireo: Bayesian demultiplexing of pooled single-cell RNA-seq data without genotype reference. Genome Biol. *20*, 273. https://doi.org/10.1186/s13059-019-1865-2.

93. Hao, Y., Stuart, T., Kowalski, M.H., Choudhary, S., Hoffman, P., Hartman, A., Srivastava, A., Molla, G., Madad, S., Fernandez-Granda, C., et al. (2024). Dictionary learning for integrative, multimodal and scalable single-cell analysis. Nat. Biotechnol. *42*, 293–304. https://doi.org/10.1038/s41587-023-01767-y.

94. Hao, Y., Hao, S., Andersen-Nissen, E., Mauck, W.M., 3rd, Zheng, S., Butler, A., Lee, M.J., Wilk, A.J., Darby, C., Zager, M., et al. (2021). Integrated analysis of multimodal single-cell data. Cell *184*, 3573–3587.e29. https://doi.org/10.1016/j.cell.2021.04.048.

95. Stuart, T., Butler, A., Hoffman, P., Hafemeister, C., Papalexi, E., Mauck, W.M., 3rd, Hao, Y., Stoeckius, M., Smibert, P., and Satija, R. (2019). Comprehensive Integration of Single-Cell Data. Cell *177*, 1888–1902.e21. https://doi.org/10.1016/j.cell.2019.05.031.

96. Butler, A., Hoffman, P., Smibert, P., Papalexi, E., and Satija, R. (2018). Integrating single-cell transcriptomic data across different conditions, technologies, and species. Nat. Biotechnol. *36*, 411–420. https://doi.org/10.1038/nbt.4096.

97. Satija, R., Farrell, J.A., Gennert, D., Schier, A.F., and Regev, A. (2015). Spatial reconstruction of single-cell gene expression data. Nat. Biotechnol. *33*, 495–502. https://doi.org/10.1038/nbt.3192.

98. Ahlmann-Eltze, C., and Huber, W. (2021). glmGamPoi: fitting Gamma-Poisson generalized linear models on single cell count data. Bioinformatics *36*, 5701–5702. https://doi.org/10.1093/bioinformatics/btaa1009.

99. Rodriguez, E.K., Hoger, A., and McCulloch, A.D. (1994). Stress-dependent finite growth in soft elastic tissues. J. Biomech. *27*, 455–467. https://doi.org/10.1016/0021-9290(94)90021-3.

100. Dobin, A., Davis, C.A., Schlesinger, F., Drenkow, J., Zaleski, C., Jha, S., Batut, P., Chaisson, M., and Gingeras, T.R. (2013). STAR: ultrafast universal RNA-seq aligner. Bioinformatics Oxf. Engl. *29*, 15–21. https://doi.org/10.1093/bioinformatics/bts635.

101. Choi, J., Joisher, H.N.V., Gill, H.K., Lin, L., and Cepko, C. (2024). Characterization of the development of the high-acuity area of the chick retina. Dev. Biol. *511*, 39–52. https://doi.org/10.1016/j.ydbio.2024.03.005.

Please cite this article in press as: Gill et al., Hox gene activity directs physical forces to differentially shape chick small and large intestinal epithelia, Developmental Cell (2024), https://doi.org/10.1016/j.devcel.2024.07.012

STAR★METHODS

KEY RESOURCES TABLE

REAGENT or RESOURCE	SOURCE	IDENTIFIER
Antibodies		
Mouse Anti-RCAS (gag-pro)	DSHB	AMV-3C2; RRID: AB_528098
Mouse Anti-alpha smooth muscle Actin antibody (Clone 1A4) (FITC-conjugated)	Abcam	ab8211; RRID: AB_306359
Mouse Anti-alpha smooth muscle Actin antibody (Clone 1A4) (Alexa Fluor® 594-conjugated)	Abcam	ab202368; RRID: AB_2924381
Rabbit Anti-Calponin 1 (Clone D8L2T)	Cell Signaling Technologies	17819; RRID: AB_2798789
Rabbit Anti-Phospho-Smad2 (Ser465/467) (Clone 138D4)	Cell Signaling Technologies	3101; RRID: AB_331673
Rabbit Anti-Collagen I antibody	Abcam	ab34710; RRID: AB_731684
Cy3 AffiniPure Donkey Anti-Mouse IgG (H+L)	Jackson ImmunoResearch	715-165-150; RRID: AB_2340813
Alexa Fluor® 647 AffiniPure Donkey Anti-Rabbit IgG (H+L)	Jackson ImmunoResearch	711-605-152; RRID: AB_2492288
Alexa Fluor® 488 AffiniPure Donkey Anti-Rabbit IgG (H+L)	Jackson ImmunoResearch	711-545-152; RRID: AB_2313584
Goat Biotin-SP (long spacer) AffiniPure Anti-Rabbit IgG (H+L)	Jackson ImmunoResearch	111-065-003; RRID: AB_2337959
Peroxidase Streptavidin	Jackson ImmunoResearch	016-030-084; RRID: AB_2337238
Chemicals, peptides, and recombinant proteins		
Recombinant Mouse TGF-beta 1 Protein	R&D Systems	7666-MB-005
Recombinant Human/Mouse/Rat Activin A Protein	R&D Systems	338-AC-010
SB431542	Selleck Chemicals	S1067
Col003	MedChem Express	HY-124817
Chick embryo extract	US Biological	C3999
Doxycycline hyclate	Millipore Sigma	D9891
DMEM	GIBCO	11960044
Pen/Strep	GIBCO	15240062
Blocking Reagent	Millipore-Sigma	11096176001
TWEEN20	Sigma Aldrich	P9416
DAPI	Roche	10236276001
Cell strainer (100 μm)	Falcon	352360
Cell strainer (40 μm)	VWR	21008-949
Trypsin-EDTA	Sigma	25200056
Round-Bottom Polystyrene Test Tubes with Cell Strainer Snap Cap, 5mL	Falcon	352235
Critical commercial assays		
TSA Plus Cyanine 3 System	Perkin Elmer	NEL744001KT
HCR™ Buffers and Amplifiers	Molecular Instruments	N/A
RNeasy Mini Kit	Qiagen	74104
Truseq Stranded mRNA Library Prep	Illumina	20020594
Truseq RNA Single Indexes Set B	Illumina	20020493
Gibson Assembly Master Mix	New England Biolabs	E2611S
Chromium Next GEM Single Cell 3' Gel Bead Kit v3.1,	10x Genomics	PN-1000122

(*Continued on next page*)

Please cite this article in press as: Gill et al., Hox gene activity directs physical forces to differentially shape chick small and large intestinal epithelia, Developmental Cell (2024), https://doi.org/10.1016/j.devcel.2024.07.012

Continued

REAGENT or RESOURCE	SOURCE	IDENTIFIER
Dual Index Kit TT Set A	10x Genomics	PN-1000125
Nextera XT DNA Sample Preparation Kit	Illumina	FC-131-1024
Deposited data		
Bulk RNA-seq data	This paper	GEO: GSE236181
scRNA-seq data	This paper	GEO: GSE258895
Light seq data	This paper	GEO: GSE260533
Experimental models: Organisms/strains		
Specific Pathogen-Free Chicken (SPF) Eggs	AVS Bio	N/A
Oligonucleotides		
Barcode sequence 1 - Cy5 labeled barcode strand.	IDT	GGAGTTGGAGTGAGTGGATGAGTGA TGDDDDDDD DDDDDTATGGATGAGT TATATAACTCA[cnvK]TCGT GTAAAT[Cy5-3]
RT.5N.3G	IDT	TTTACACGATTGAGTTATNNNNNGGG
GATC.20T	IDT	GAGAATGTGAGTGAAGATGTATGGTG ATTTTTTTTT TTTTTTTTTT
GATE	IDT	GGAGTTGGAGTGAGTGGATGAGTGATG
GATC	IDT	GAGAATGTGAGTGAAGATGTATGGTGA
P5.GATE	IDT	CGCCGGAGTTGGAGTGAGTGGATGAGTGATG
GATE*.P5*	IDT	CATCACTCATCCACTCACTCCAACTCCGGCG
Recombinant DNA		
Chick *HOXD13* CDS (codon-optimized)	IDT	N/A
pPIDNB	Chu et al.[80]	Addgene Plasmid #169901
pPB[Exp]-Puro-CAG>hyPBase	Vector Builder	Cat#: VB900097-3203ztc
pPIDNB-*HOXD13*	This paper	N/A
RCAS-*HOXD13*	Roberts et al.[19]	N/A
RCAS-*mGFP*	Kan et al.[77]	N/A
Chick *INHBA* probe set	Molecular Instruments	N/A
Chick *CFC1* probe set	Molecular Instruments	N/A
Chick *THBS2* probe set	Molecular Instruments	N/A
Chick *HOXD13* probe set	Molecular Instruments	N/A
Chick *FBLN1* probe set	Molecular Instruments	N/A
Chick *VCAN* probe set	Molecular Instruments	N/A
Chick *TAGLN* probe set	Molecular Instruments	N/A
Software and algorithms		
ImageJ	NIH	https://imagej.nih.gov/ij/
GraphPad Prism 9	GraphPad	https://www.graphpad.com/scientific-software/prism/
MATLAB R2023b	Mathworks	https://www.mathworks.com/products/matlab.html
ABAQUS/Standard 6.14	Dassault Systemes	https://www.3ds.com/products/simulia/abaqus/standard
R 4.2.0	R Core Team	https://cloud.r-project.org/
STAR	Dobin et al.[100]	https://github.com/alexdobin/STAR
Salmon	Patro et al.[86]	https://github.com/COMBINE-lab/salmon
DESeq2	Love et al.[85]	https://doi.org/10.18129/B9.bioc.DESeq2
Seurat 4.3.0	Butler et al.[96]; Stuart et al.[95]	https://github.com/satijalab/seurat
Cellranger (7.1.0)	10x Genomics	https://www.10xgenomics.com/support/software/cell-ranger/downloads
Demultiplex	McGinnis et al.[91]	https://github.com/chris-mcginnis-ucsf/MULTI-seq
glmGamPoi	Ahlmann-Eltze and Huber[98]	http://bioconductor.org/packages/release/bioc/html/glmGamPoi.html

(*Continued on next page*)

Please cite this article in press as: Gill et al., Hox gene activity directs physical forces to differentially shape chick small and large intestinal epithelia, Developmental Cell (2024), https://doi.org/10.1016/j.devcel.2024.07.012

Continued

REAGENT or RESOURCE	SOURCE	IDENTIFIER
Lightseq	Kishi et al.[50]	https://github.com/Harvard-MolSys-Lab/Light-Seq-Nature-Methods-2022
Code for image analysis, mechanical measurements, and sequencing analysis	This paper	Zenodo: https://github.com/hasreetkgill/Hoxd13-manuscript
Code for numerical simulations	This paper	Zenodo: https://doi.org/10.5281/zenodo.12687202; https://github.com/YinSifan0204/GutMorphology_3DSimulations
Code for radial pattern quantification	Huycke et al.[37]	https://github.com/dsprinzak/huycke-et-al-Cell-2019
Code for spatial order analysis	Choi et al.[101]	https://github.com/hasreetkgill/opsinanalysis

RESOURCE AVAILABILITY

Lead contact

Further information and requests for resources and reagents should be directed to and will be fulfilled by the lead contact, Clifford J. Tabin (tabin@genetics.med.harvard.edu).

Materials availability

Plasmids generated in this study will be provided by the lead contact upon request.

Data and code availability

- Bulk, single cell, and light-seq RNA-sequencing data have been deposited at GEO and are publicly available. Accession numbers are listed in the key resources table. Microscopy data reported in this paper will be shared by the lead contact, Clifford J. Tabin (tabin@genetics.med.harvard.edu), upon request.
- All original codes have been deposited at Zenodo and are publicly available. The DOIs and associated Github links are listed in the key resources table.
- Any additional information required to reanalyze the data reported in this paper is available from the lead contact upon request.

EXPERIMENTAL MODEL AND STUDY PARTICIPANT DETAILS

All animal studies were performed in compliance with NIH guidelines and standard operating protocols approved by the Institutional Animal Care and Use Committee at Harvard Medical School.

Chickens

Fertilized Specific Pathogen Free (SPF) White Leghorn Chicken eggs (AVS Bio) were incubated in a 38°C humidified chamber. Embryonic stages are indicated in figures and figure legends, and were determined using the Hamburger and Hamilton staging series.[76] Sex was only noted using NGS data and considered during single cell RNA-sequencing analysis, but was otherwise not accounted for due to the technical difficulty of determining sex from chicken embryos.

METHOD DETAILS

Plasmids

The full-length chick HOXD13 CDS sequence (NCBI gene ID: 396415) was codon optimized and ordered as a gBlock Gene Fragment (IDT) with 5' and 3' sequences complementary to the destination vector for isothermal assembly. It was then cloned into the pPIDNB backbone vector (Addgene plasmid #169901; a gift from Richard Schneider) digested with AflII and PstIII to create pPIDNB-*HOXD13*. RCAS-*HOXD13*[19] and RCAS-*mGFP*[77] were obtained from lab stocks. hyPBase was ordered from VectorBuilder (pPB[Exp]-Puro-CA-G>hyPBase, ID: VB900097-3203ztc).

Chick intestinal electroporation

Expression constructs were electroporated into the midgut splanchnic lateral plate at HH17, as described in detail previously.[37] Because RCAS viral particles do not cross the basement membrane, this method ensured tissue-specific misexpression in the mesoderm (Figure S2C).[37,78,79] RCAS constructs were electroporated at a concentration of 2.5μg/μL, where hindgut and midgut controls were electroporated with RCAS-*mGFP* or obtained from stage-matched non-electroporated embryos. Successful viral spread was confirmed using whole-mount AMV-3C2 (1:100, DSHB) immunostaining. pPIDNB/pPIDNB-*HOXD13* were co-electroporated with hyPBase at concentrations of 3μg/μL and 1μg/μL, respectively.[80]

Please cite this article in press as: Gill et al., Hox gene activity directs physical forces to differentially shape chick small and large intestinal epithelia, Developmental Cell (2024), https://doi.org/10.1016/j.devcel.2024.07.012

Sparse, inducible HOXD13 expression

pPIDNB-*HOXD13* undergoes transposon-mediated integration into the genomes of electroporated cells, which then constitutively express mNeonGreen under a PGK promoter.[80] Upon doxycycline exposure, expression of both *mScarlet* and *HOXD13* is induced from a bidirectional TRE element (Figure S6A).

To induce expression of *mScarlet* and *HOXD13* from pPIDNB-*HOXD13*, 750μL of a 3.3μg/μL solution of doxycycline hyclate (Millipore Sigma; 1mg/mL stock in water) in HBSS was filter sterilized and gently pipetted on top of electroporated/windowed E8 embryos.[80] Windows were then re-sealed, and embryos were incubated for another 7 days. The same procedure was performed for pPIDNB-electroporated controls to induce *mScarlet* expression alone.

Lumen surface imaging

Surface relief structures of intestinal segments were imaged by first dissecting and longitudinally slicing gut tubes in 1X PBS. Opened guts were then pinned flat (without stretching) to 3% agarose using 0.002-inch or 0.004-inch diameter tungsten rods, and submerged in 4% PFA for fixation at 4°C overnight, or at room temperature for 1-2 hours. Fixed guts were stained with DAPI in 1X PBS overnight at 4°C and imaged on a Zeiss LSM 710 point-scanning inverted confocal microscope. Maximum projections of, depending on stage and region, approximately 20-60μm Z stacks at 2-5μm step size were generated using ImageJ. Transverse section images were taken using a Nikon Ti2 inverted W1 Yokogawa Spinning disk microscope (50μm pinhole disk). 10μm Z stacks at 0.5-1μm step size were also analyzed as maximum projections.

Surface wrinkling quantification

Pattern analysis of lumen surface images was performed using a combination of custom and adapted pipelines in MATLAB. For Fast Fourier Transforms (FFTs), we first applied a series of pre-processing operations to DAPI channel maximum projections using MATLAB. These generally involved a Gaussian filter followed by adaptive thresholding before binarization of the image. Power spectra in the frequency domain were obtained from the log of the absolute value of the 2D FFT (fft2 function) performed on binary images. Spatial domain images that displayed periodic patterns showed distinct peaks in their corresponding power spectral density profiles, while non-periodic patterns had diffuse power spectra. Cases with notable peaks within figures are marked with the characteristic wavelength values on the relevant axis or axes.

To count branched folds, 180x180μm^2 sample areas were randomly selected and cropped from a whole-lumen image (hindgut and explants), or a 2-3 mm gut segment lumen (midgut). Images were binarized and skeletonized, and branch points were scored manually using the point selection tool in ImageJ.

Autocorrelation profiles were obtained by first cropping raw midgut images in x and y to isolate a representative segment of the periodic pattern. The dimensions of this segment varied between stages but not between conditions (midgut, hindgut, RCAS-*HOXD13* midgut). Autocorrelation was calculated using the MATLAB autocorr function applied to a vector containing the 1D signal intensity pattern of the cropped image.[81] The presence of a sinusoidal wave in the resulting plot indicates periodicity as a correlation between DAPI intensity at a given point in the source image, going from left to right, with intensities at prior points. Non-periodic patterns result in low-amplitude or flat curves. For each sinusoidal pattern, amplitude was measured as the average amplitude of the first 2 waves of the autocorrelation plot.

For spatial disorder, we used Delaunay triangulation and Voronoi cell analysis, where center points of primordial villi and cuffs were manually extracted in MATLAB, and the delaunay and voronoi functions were used to generate tessellations. Variances were calculated from distributions of triangle edge lengths and Voronoi cell areas. Higher variances of Delaunay triangle edge length and Voronoi cell area distributions correspond to higher spatial disorder.

Fold aspect ratio quantification

Geometric properties of mucosal folds at E14 and E18 were measured manually, from transverse section images in the DAPI channel. Aspect ratios were measured from randomly sampled mucosal folds taken from transverse sections. The bottom of a fold was defined as the average radial position of the valleys on either side of a protrusion, and the top of a fold was the radial position located closest to the lumen center; width was measured orthogonally across the fold at the radial position halfway between these points.

Section immunostaining and quantification

Tissues fixed overnight in 4% paraformaldehyde in 1X PBS (PFA) were washed, dehydrated in 30% sucrose in 1X PBS and embedded in OCT blocks. Using a cryostat, guts were sectioned onto Superfrost slides as 16μm thick slices and allowed to dry completely. Tissues were permeabilized with PBSTT (1X PBS + 0.1% Tween-20 + 0.05% Triton-X100) prior to application of primary antibodies at 4°C overnight. The following primary antibodies were used: αSMA-FITC (1:1000, Sigma), αSMA-A594 (1:1000, Abcam), calponin 1 (1:100, Cell Signaling), phospho-SMAD2 (1:300, Cell Signaling), and collagen I (1:300, Abcam). All secondary antibodies were added 1:300 in PBSTT at room temperature for 2 hours. Secondary antibodies conjugated to fluorescent dyes were chosen with regard to primary antibody species (1:300, Jackson Immuno, 1:300). For phospho-SMAD2 stains, antigen retrieval was performed by boiling slides for 5min in pH 6.0 citrate buffer using a veggie steamer prior to antibody application. TSA signal amplification was then performed according to kit recommendations (Perkin Elmer) following a biotinylated anti-rabbit secondary incubation (1:300,

Please cite this article in press as: Gill et al., Hox gene activity directs physical forces to differentially shape chick small and large intestinal epithelia, Developmental Cell (2024), https://doi.org/10.1016/j.devcel.2024.07.012

Jackson Immuno) and a streptavidin-HRP incubation (1:300, Jackson Immuno). Proportion of pSMAD2+ nuclei were counted in ImageJ from a single z-slice by first segmenting the subepithelial mesenchyme (area between white lines in Figure 3F), followed by manual counting in the DAPI and pSMAD2 channels.

Fluorescence in situ hybridization

sm*FISH* using HCR was performed using reagents and an adapted protocol from Molecular Instruments.[82] Sections on slides were washed with 1X PBS and permeabilized for 2 hours in 70% ethanol. After a short pre-incubation in Hybridization Buffer at 37°C, custom probes from 1μM stocks were mixed with pre-warmed Hybridization Buffer to a final concentration of 6nM. Probe solutions were added to slides and coverslips cut from polypropylene bags were applied before placing slides in a humidified chamber at 37°C for 18 hours. The following probe sets were manufactured by Molecular Instruments from the associated sequence IDs: *INHBA* (NM_001396543.1), *CFC1* (NM_204700.3), *THBS2* (NM_001397325.1), *HOXD13* (NM_205434.1), *FBLN1* (NM_204165.1), *VCAN* (NM_204787.1), *TAGLN* (NM_205494.2). Excess probes were washed at 37°C using 30 minute washes in 4 graded concentrations of probe wash buffer (Molecular Instruments)/5X SSCT (5X SSC buffer + 0.1% Tween-20), followed by 2 washes in 5X SSCT at room temperature. H1 and H2 hairpins from 3μM stocks (Molecular Instruments) were separately heated to 95°C in a heat block and allowed to reanneal at room temperature for 30 minutes in the dark. Hairpins were then mixed with amplification buffer (Molecular Instruments) at a final concentration of 50nM and incubated in the dark for 5 minutes. The hairpin solutions were added to slides, which were covered with polypropylene coverslips and incubated at room temperature for 20 hours. Samples were then washed with 5X SSCT to remove excess hairpins, stained with DAPI in 1X PBS, and mounted for imaging. Radial quantification of signal intensity for immunostains and *FISH* patterns was performed as described previously,[37] where x-positions were normalized to the total average thickness of the mesenchyme for each condition, and y-axis normalized to maximum intensity. Large, irregular bright spots in HCR-*FISH* images are auto-fluorescent enteric neural crest cells.

Mechanical measurements

Thickness ratio, differential growth and Young's modulus measurements were collected as described in Gill et al.[26] Briefly, thicknesses were measured from fixed 16μm transverse sections stained with DAPI and smooth muscle markers (Figures 2A and S1A). For growth and modulus measurements, tissue layers were dissected in 1X PBS at room temperature using electrolytically sharpened rods. For differential growth, the composite of endoderm and mesenchyme was dissected from the circumferential layer of smooth muscle. Tissues were allowed to reach their stress-free lengths for 20min before strain was determined as the percent increase or decrease in tissue length in the relaxed configuration.[25,26,83,84] In Figures 5D and 6F, growth anisotropy was measured as the difference between the change in longitudinal and circumferential strain magnitude ($\Delta\epsilon$) over the course of the experiment. Initial strains corresponded to E12 strains shown in Figure 2B.

For modulus testing, tissue rings were imaged while stretched at a constant velocity using a tungsten cantilever hooked through the lumen (Figure S1A). Deformation in the tissue and deflection of the cantilever were used to measure Young's modulus.[26] For guts older than 14 days for the midgut and hindgut, and 16 days for the *HOXD13*-misexpressing midgut, tissue layers were too thin to dissect for modulus measurements. Modulus ratios were therefore inferred by fitting a curve to data from several earlier stages (Figure S1D).

Bulk RNA sequencing

Lumen patterns become distinct across conditions from E12 to E14, so we collected tissue from the midgut, hindgut, and *HOXD13*-expressing midgut at these times. Also, because *HOXD13* misexpression was restricted to the mesoderm and mechanical changes occurred mainly in the mesenchyme layer, we only harvested mesodermal RNA (Figures S1B, S1C, and S2C).

Whole guts were dissected from electroporated embryos in fresh, ice-cold 1X PBS. 4 replicates of RCAS-*mGFP* midguts, RCAS-*mGFP* hindguts, and RCAS-*HOXD13* midguts were collected for each time point. RCAS-*mGFP* midguts and hindguts were obtained from the same individuals. To harvest tissue samples of roughly equivalent mass, 2-3mm hindgut segments and 3-4mm midgut segments were isolated and immediately cut open longitudinally. Samples were then placed in Eppendorf tubes containing 1mL of 2Units/μL dispase in 1X PBS and incubated on a rocker at 37°C for 10 minutes. Segments were transferred to a new dish of 1X PBS and the inner epithelium was carefully peeled away using fine forceps. Remaining mesodermal tissue was kept on ice until all tissues were collected. RNA was extracted using the QIAGEN RNeasy Micro Kit. All E12 samples were collected simultaneously, and E14 samples were collected in 4 batches with 1 replicate of each condition collected per batch. RNA quality was assessed using an Agilent 2100 Bioanalyzer. Libraries were prepared from 500ng input RNA using the Illumina TruSeq Stranded mRNA kit and pooled separately for E12 and E14 prior to sequencing.

For sequencing, single end 75bp reads were sequenced on a NextSeq 500 flowcell at the Biopolymers Facility at Harvard Medical School. For the RCAS-*mGFP* midgut, RCAS-*mGFP* hindgut, and RCAS-*HOXD13* midgut, average reads per replicate generated by E12 libraries were 13.3, 14.0, and 14.0 million, respectively. Average reads per replicate for E14 libraries were 14.2, 14.5, and 13.4 million, respectively. Reads were quasi-mapped to the reference chick transcriptome using Salmon,[85] and the Salmon pseudocount matrix was used for differential gene expression analysis in R using DESeq2.[86] Hierarchical clustering was performed to identify differentially expressed genes commonly shared between RCAS-*mGFP* midgut vs. RCAS-*HOXD13* midgut and RCAS-*mGFP* midgut vs. RCAS-*mGFP* hindgut. To identify differentially regulated pathways, we analyzed lists of commonly differentially expressed genes between comparisons using the free online suite of gene set enrichment tools, EnrichR[87–89] (Figure S4B). After identifying TGFβ as a

Please cite this article in press as: Gill et al., Hox gene activity directs physical forces to differentially shape chick small and large intestinal epithelia, Developmental Cell (2024), https://doi.org/10.1016/j.devcel.2024.07.012

pathway of interest, the KEGG 2021 and BioPlanet 2019 lists of TGFβ signaling pathway genes were used to sub-classify genes as they are represented in Figure 3.

Volcano plots and heatmaps were generated using R. In Figures 3A and 3B, of genes also up- or down-regulated in the RCAS-*HOXD13* midgut vs. control midgut (darker gray dots), a proportion were commonly differentially expressed at both points (green triangles), and a subset of those were genes known to be involved in the TGFβ pathway (pink diamonds and gene name labels). Dashed gray lines indicate the significance cutoff at adjusted p=0.05.

Single cell RNA sequencing

Single cell suspensions were generated by first dissecting guts in ice-cold 1X PBS. Whole guts were placed in DMEM + 10% chick embryo extract at 37°C until all samples were dissected and ready for dissociation. For pPIDNB experiment samples, dissected guts were observed under epifluorescence to isolate regions with mScarlet+ transgenic cells. 2-3mm gut segments, 1 from each replicate, were then incubated at 37°C in 1mL dispase for 10min as for bulk RNA sequencing sample preparation, followed by 1 PBS wash. Gut pieces (pooled by condition) were placed in the open caps of Eppendorf tubes containing 500μL 0.25% Trypsin-EDTA (Sigma) and mechanically disrupted using forceps. Tubes were then closed and inverted before placing samples at 37°C for 12-15min. Samples were mechanically disrupted with P1000 and P200 pipettes every 2min during the first half of the incubation, and with a 1mL syringe/25G needle during the second half.

When pPIDNB midgut, pPIDNB-*HOXD13* midgut, and electroporated control hindgut suspensions were homogenous with no visible tissue clumps, 400μL of ice cold DMEM + 4% FBS was added to each sample, which was then strained using a 5mL polystyrene round-bottom tube with a 35μm nylon mesh cell strainer cap (Falcon). After one spin at 800xg for 5min at 4°C, samples were resuspended in DMEM + 4% FBS, labeled for 5min with DAPI, and placed on ice. To enrich for mScarlet+ cells, midgut samples were iteratively sorted 3 times for approximately 30min each using an On-chip Sort microfluidic chip sorter.[90] The mScarlet+ mNeon+DAPI- population was gated to select for living cells with induced transgene expression. Trypan blue staining before and after all samples were sorted confirmed minimal cell death due to time spent on ice. After straining again through a 70μm mesh strainer and cell counting using a hemocytometer, sorted suspensions in 1X PBS were used for GEM generation according to the 10X Chromium Next GEM Single Cell v3.1 (Dual Index) protocol. Subsequent post GEM-RT cleanup, cDNA amplification, and 3' gene expression library construction steps were performed in accordance with the manufacturer's instructions. Sample indices were chosen from the 10X Dual Index Kit TT Set A (PN-1000215).

For wild-type E14 midgut and hindgut samples, the 500μL trypsin suspension was strained without the addition of FBS. After straining, samples were centrifuged at 800xg for 5min, followed by 2 PBS washes. Midgut and hindgut suspensions were then barcoded for MULTI-seq, washed twice with ice-cold PBS + 1% BSA, and pooled.[91] Cells were then strained, counted, and used in the 10X workflow for GEM generation and library preparation as described above. During the SPRI bead cleanup step following cDNA amplification, the supernatant was preserved and used to generate MULTI-seq barcode libraries, which were also sequenced and used together with the genotype-based demultiplexing using vireo[92] to computationally infer the sample origin of midgut and hindgut cells during data processing.[91]

Paired-end (28/8/10/90 dual index) sequencing was performed on a NovaSeq 6000 flowcell at the Biopolymers Facility at Harvard Medical School according to the recommended 10X sequencing specification. Cellranger 7.1.0 was used to generate the count matrix, which by default, include all counts of intronic reads. Parsing of cellular barcodes, MULTI-seq barcodes, and genotype-based demultiplexing using vireo were all performed on the Harvard Medical School O2 computing cluster.

After generation of Seurat objects, downstream analysis using the Seurat package was performed in R version 4.2.1.[93–97] Graph-based clustering and non-linear dimensional reduction in Seurat were performed for each dataset using the Leiden algorithm and UMAP, with the number of dimensions used determined from each elbow plot inflection point. Integration of datasets from the same experiment was performed using the CCA method available in the Seurat package, and pseudobulk differential gene expression used the glmGamPoi package.[98] Design formulas for differential expression regressed out variation due to sex and cell cycle phase. In cases where only a particular cell subtype comprising multiple clusters (e.g., "Mesenchyme") is considered, cell type annotations were determined after dataset integration to ensure equivalent matching of cell populations between conditions, and the original data was subsetted and re-clustered accordingly. Finally, for pPIDNB empty vector control embryos, though mScarlet+ cells were sorted and enriched as for pPIDNB-*HOXD13* embryos, *mScarlet* expression level was too low for pseudo-bulking as part of differential expression analysis; therefore, *mNeon*+ cells were used for comparison to *HOXD13*+ cells instead ("Mid cells" and "Mid control" cells in Figures 3C, S5B, and S5E), as we observed no major transcriptional differences between *mScarlet*+ and *mNeon*+ cells in control samples.

Chick intestinal explant culture

2-3mm segments of E12 midguts and E13 hindguts were dissected in pre-warmed 1X DMEM containing 1% Pen/Strep and transferred to 6-well dishes with 2 segments per dish. All explants were cultured in 1X DMEM containing 1% Pen/Strep and 10% chick embryo extract. Enough media was added to each dish such that guts were at the air-liquid interface, which ranged from 800μL to 1mL depending on the size of the tissue. Dishes were then placed on a rocker at approximately 12 rocks per minute, within a 37°C incubator with 5% CO_2 and 19% O_2. Media was changed every 24 hours for 72 hours of culture. Final morphologies of control midgut and hindgut cultures were close approximations of their *in ovo* counterparts, with midguts forming modest zigzags from initial ridges and hindguts forming sulci from flat surfaces (Figures 5A and 5B). The following stock solutions of pharmacological compounds were

Please cite this article in press as: Gill et al., Hox gene activity directs physical forces to differentially shape chick small and large intestinal epithelia, Developmental Cell (2024), https://doi.org/10.1016/j.devcel.2024.07.012

made, stored at -20°C, and diluted before adding to media at 0.1% to achieve final concentrations indicated in figure legends: recombinant mouse TGFβ1 (50μg/mL in 1X PBS + 4mM HCL + 0.1% BSA, R&D Systems), Activin A (10μg/mL in 1X PBS + 4mM HCL + 0.1% BSA, R&D Systems; final concentration 10ng/mL), SB431542 (20mM in DMSO), Col003 (50mM in DMSO). An equivalent volume of vehicle was added to each control—for experiments employing compounds dissolved in different solvents, an equivalent volume of each solvent was added to a single set of controls.

Light-seq spatial RNA sequencing

Light-seq was performed according to the methodology described in Kishi et al.[50] Tissues were collected and fixed for 1hr at room temperature in 4% PFA with 0.1% Tween-20, followed by 1X PBS washes, a 1hr incubation in 30% sucrose, and 1hr in 100% OCT. 2-3mm gut segments were embedded in OCT blocks and sectioned sagittally onto Superfrost slides coated with poly-D-lysine (Sigma, 0.3mg/mL in Borate Buffer). Square plastic chambers were then superglued on top of sections for subsequent reactions. Samples were washed with PBS followed by PBST (1X PBS + 0.1% Tween-20), before completing *in situ* reverse transcription of RNA using a 12-cycle ramp program, which added 5N3G sequences onto cDNA strands for eventual crosslinking to barcodes.[50] A-tailing was performed for 45 minutes at 37°C, followed by overnight incubation in αSMA-A594 primary antibody.

Samples were barcoded using a Mightex Polygon 400 DP DMD attached to an inverted Nikon Eclipse Ti-E. Sections were incubated in 1M NaCl followed by barcoding solution (PBST containing 2mg/mL sheared salmon sperm DNA, 10% dextran sulfate, 250nM Barcode I strand, and 500mM NaCl) for 30min at room temperature. After PBS + NaCl washes, tissue regions were outlined using the Bezier ROI tool in Nikon Elements v.4.51. DMD illumination of each ROI (1 per replicate) was performed on a single z-plane to cross-link barcodes onto cDNAs in the tissue (Figure S7C). For the midgut, hindgut, and RCAS-*HOXD13* midgut, a portion of subepithelial mesenchyme was outlined, starting from the basement membrane to the center of the inner longitudinal layer of smooth muscle (Figure S7C). Basement membrane location was determined using DAPI, and the inner longitudinal layer was identified using αSMA-A594 staining. The total area illuminated per section varied from 20,000-80,000μm^2 depending on tissue identity, as the mesenchyme layer is thicker in the hindgut and midgut + *HOXD13*. An Cy5-labeled barcode was used for the subepithelial mesenchyme, and successful barcoding was confirmed using a fluorescence widefield microscope. Following washes with PBST+60% deionized formamide, barcoded cDNAs were displaced from samples, and cross-junction synthesis reactions were performed to stitch barcoded cDNAs into single strands. DNA was then amplified using PCR, purified using Ampure XP beads (Beckman), and concentrations were quantified using a Qubit assay.

Sequencing libraries were prepared using a Nextera XT Library Preparation Kit (Illumina). Tagmentation was performed using a custom i5 primer,[50] and libraries were pooled and sequenced with custom Read 1 and i5 primers. Sequencing was performed using a NextSeq 500 machine at the Biopolymers Facility at Harvard Medical School. For analysis, barcode and UMI sequences were extracted from raw Read 1 data using the UMI-tools package, and sequences were mapped to the galgal6 (GRCg6a, Ensembl) chicken genome assembly using STAR. UMI deduplication and barcode parsing was performed in Python (3.7.5).[50] Differential gene expression analysis was performed in R using DESeq2.[85]

Numerical simulations

To simulate late-stage ridge, zigzag, sulci, and cuff formation, we first adapted our two-dimensional growing bilayer model of early buckling initiation to three dimensions.[26] Briefly, tissues were modeled as Neo-Hookean elastic solids, and growth was modeled as a shift in the stress-free reference configuration prescribed along three orthogonal axes according to the residual strain measurements.[99]

To perform 3D simulations, we implemented a user-defined material (UMAT/VUMAT) subroutine in the commercial finite program ABAQUS/Standard (version 6.14). Three biophysical parameters are defined in the initial stress-free state in ABAQUS: the thickness ratio and modulus ratio of the endodermal and mesenchymal layers, and the radius ratio of the inner (center to apical side of the endoderm) and outer (center to inner boundary of the circumferential layer) radii of the endoderm-mesenchyme composite. While thickness and modulus ratios were fitted to the data, the radius ratio was kept as 0.65 for all simulations. To simplify the process of phase diagram construction, experimental data were binned such that simulation parameters do not perfectly match, but closely approximate, actual or predicted values (Table S1). 27 simulations were performed in total to create the diagram in Figure 2F. In a tubular geometry, views depicted correspond to the basal surface of the endoderm layer for ease of visualizing the morphology. The bidirectional arrow on the bottom right in Figures 2F and 5H indicates orientation of differential growth on a spectrum from isotropic (green) to anisotropic (pink). Blue "sulci" and orange "cuff-like" colored morphological domains were defined empirically using isotropic growth simulations. For cases with anisotropic growth (pink axis), "θ" and "z" above the boxes represent dominant growth directions.

The stepwise anisotropic growth profile of the midgut and the transversely isotropic growth profile of hindgut were based on experimental results. The following sets of growth functions were developed to be qualitatively consistent with the data and were applied to simulation conditions as specified in Table S1.

Stepwise anisotropic

$$g_r = 1$$

Please cite this article in press as: Gill et al., Hox gene activity directs physical forces to differentially shape chick small and large intestinal epithelia, Developmental Cell (2024), https://doi.org/10.1016/j.devcel.2024.07.012

$$g_\theta = 1 - t^2 + 2t$$

$$g_x = 1 + 2t^2$$

Stepwise anisotropic with endoderm thinning

$$g_r = 1 - 0.5t$$

$$g_\theta = 1 - 2t^2 + 4t$$

$$g_x = 1 + 4t^2$$

Transversely isotropic

$$g_r = 1$$

$$g_\theta = g_x = 1 + t$$

Transversely isotropic with endoderm thinning

$$g_r = 1 - 0.5t$$

$$g_\theta = g_x = 1 + t$$

Circumferential anisotropic

$$g_r = 1$$

$$g_\theta = 1 + 2t^2$$

$$g_x = 1$$

In contrast to our previous computational model for the wild-type midgut,[25] here we used UMAT and the implicit method to ensure the slow formation of ridge and zigzag patterns (occurring over the course of several days in the embryo) reaches mechanical equilibrium at every time step; for the hindgut, we used VUMAT and the explicit method to mimic the process of sulci (creasing) and cuff formation, which occurs embryonically in the span of hours, and thus relatively quickly (Table S1). Evolution of the RCAS-*HOXD13* midgut morphology was initially simulated using the implicit method to reflect its deviation from the ridge-to-zigzag to a ridge-to-sulci transition. Simulations of later stage wrinkling, which mimics that of the hindgut, employed the explicit method for comparison to the hindgut. The same principle was applied to the choice of implicit vs. explicit models for explant experiment simulations (Table S1).

QUANTIFICATION AND STATISTICAL ANALYSIS

Statistical tests were performed using Excel and GraphPad Prism, and statistical details for each experiment reported can be found below for Figures 1, 2, 3, 4, 5, and 6 and in the figure legends for Figures S1–S7. For mechanical measurements and lumen quantifications in Figures 1, 2, 5, S1, S3, and S6, populations were assumed to be sufficiently normally distributed with similar standard deviations, and thus ordinary one- or two-way ANOVAs and unpaired, two-tailed t-tests were performed. Multiple testing correction was performed after ANOVA tests as part of Tukey's pairwise comparison tests (Tukey's MCT), and for NGS data using the Bonferroni or the Benjamini-Hochberg (BH) method (indicated in figure legends). In all cases where asterisks indicate significance, the following convention was used: *****, p<0.00001; ****, p<0.0001; ***, p<0.001; **, p<0.01; *, p<0.05; ns, not significant. Standard errors are reported in all cases involving comparisons between means, and standard deviation is reported for normalized autocorrelation and radial intensity profiles to illustrate spread amongst samples. Error propagation was used to determine the uncertainty of mesenchyme modulus, modulus ratio, and growth anisotropy values. Since composite modulus, endoderm modulus, endoderm thickness, composite thickness, and mesenchyme thickness are all correlated variables, mesenchyme modulus error was propagated from composite modulus error, modulus ratio error (σ) was calculated as $\sigma_{\frac{E_e}{E_m}} = \frac{\overline{E_e}}{\overline{E_m}}\sqrt{\left(\frac{\sigma_{E_e}}{\overline{E_e}}\right)^2 + \left(\frac{\sigma_{E_m}}{\overline{E_m}}\right)^2}$, and growth anisotropy error was calculated as $\sigma_{E_e/E_m} = \sqrt{(\sigma_{\Delta\varepsilon_z})^2 + (\sigma_{\Delta\varepsilon_\theta})^2}$.

Please cite this article in press as: Gill et al., Hox gene activity directs physical forces to differentially shape chick small and large intestinal epithelia, Developmental Cell (2024), https://doi.org/10.1016/j.devcel.2024.07.012

Results for statistical tests for each Figure are as follows: Figures 1F and 1G (One-way ANOVA, branched folds: $p<0.0001$, $F=294$; aspect ratio: $p=0.006$, $F=6.41$), Figures 2B and 2C (Two-way ANOVA, conditions: $p_{\theta}<0.0001$, $F_{\theta}=15.5$; $p_z=0.071$, $F_z=3.26$; $p_{he/hm}=0.044$, $F_{he/hm}=4.03$, and stages: $p_{\theta}<0.0001$, $F_{\theta}=45.3$; $p_z<0.0001$, $F_z=59.1$; $p_{he/hm}<0.0001$, $F_{he/hm}=52.3$), Figure 2D (One-way ANOVA at E14, $p=0.0005$, $F=27.3$), Figure 3G (One way ANOVA, E12: $p=0.0002$, $F=66.9$; E14: $p=0.062$, $F=4.57$), Figures 6D–6F (One-way ANOVA, branched folds: $p<0.0001$, $F=76.8$; $p_{Ee/Em}=0.02$, $F_{Ee/Em}=8.03$; $p_{he/hm}=0.0128$, $F_{he/hm}=7.35$; growth anisotropy: $p=0.102$, $F=2.97$).